

Magnetic Perturbation Events (MPEs) that cause GICs: Investigating their Interhemispheric Conjugacy and Control by IMF Orientation

Engebretson Mark J.¹, Simms Laura E.¹, Pilipenko Vyatcheslav A.², Bouayed Lilia¹,
Moldwin Mark B.³, Weygand James M.⁴, Hartinger Michael D.⁵, Xu Zhonghua⁶, Clauer C.
Robert⁶, Coyle Shane⁷, Willer Anna⁸, Freeman Mervyn P.⁹, and Gerrard Andrew J.¹⁰

¹Department of Physics, Augsburg University

²Institute of Physics of the Earth

³University of Michigan-Ann Arbor

⁴Department of Earth, Planetary, and Space Sciences

⁵Space Science Institute

⁶Virginia Polytechnic Institute and State University

⁷Virginia Tech

⁸Technical University of Denmark

⁹British Antarctic Survey

¹⁰New Jersey Institute of Technology

November 16, 2022

Abstract

Nearly all studies of impulsive magnetic perturbation events (MPEs) that can produce dangerous geomagnetically induced currents (GICs) have used data from the northern hemisphere. In this study we investigated MPE occurrences during the first 6 months of 2016 at four magnetically conjugate high latitude station pairs using data from the Greenland West Coast magnetometer chain and from Antarctic stations in the conjugate AAL-PIP magnetometer chain. Events for statistical analysis and four case studies were selected from Greenland/AAL-PIP data by detecting the presence of >6 nT/s derivatives of any component of the magnetic field at any of the station pairs. For case studies, these chains were supplemented by data from the BAS-LPM chain in Antarctica as well as Pagnirtung and South Pole in order to extend longitudinal coverage to the west. Amplitude comparisons between hemispheres showed a) a seasonal dependence (larger in the winter hemisphere), and b) a dependence on the sign of the B_y component of the interplanetary magnetic field (IMF): MPEs were larger in the north (south) when IMF B_y was > 0 (< 0). A majority of events occurred nearly simultaneously (to within ± 3 min) independent of the sign of B_y as long as $|B_y| \geq 2 |B_z|$. As has been found in earlier studies, IMF B_z was < 0 prior to most events. When IMF data from Geotail, Themis-B, and/or Themis C in the near-Earth solar wind were used to supplement the time-shifted OMNI IMF data, the consistency of these IMF orientations was improved.

Journal of Geophysical Research - Space Physics Supporting Information for

**Magnetic Perturbation Events (MPEs) that cause GICs:
Investigating their Interhemispheric Conjugacy and Control
by IMF Orientation**

Mark J. Engebretson¹, Laura E. Simms^{1,2}, Viacheslav A. Pilipenko^{1,3}, Lilia Bouayed^{1,4}, Mark B. Moldwin², James M. Weygand⁵, Michael D. Hartinger⁶, Zhonghua Xu⁷, C. Robert Clauer⁷, Shane Coyle⁷, Anna N. Willer⁸, Mervyn P. Freeman⁹, and Andy J. Gerrard¹⁰

¹Department of Physics, Augsburg University, Minneapolis, MN

²Department of Climate and Space Sciences and Engineering, University of Michigan, Ann Arbor, MI

³Space Research Institute, Moscow, Russia

⁴Now at the Department of Physics, University of Minnesota, Minneapolis, MN

⁵Department of Earth, Planetary and Space Sciences, University of California, Los Angeles, CA

⁶Space Science Institute, Boulder, CO

⁷Bradley Department of Electrical and Computer Engineering, Virginia Polytechnic Institute and State University, Blacksburg, VA

⁸DTU Space, Kongens Lyngby, Denmark

⁹British Antarctic Survey, Cambridge, UK

¹⁰Department of Physics, New Jersey Institute of Technology, Newark, NJ

Contents of this file

Figures S1 – S5

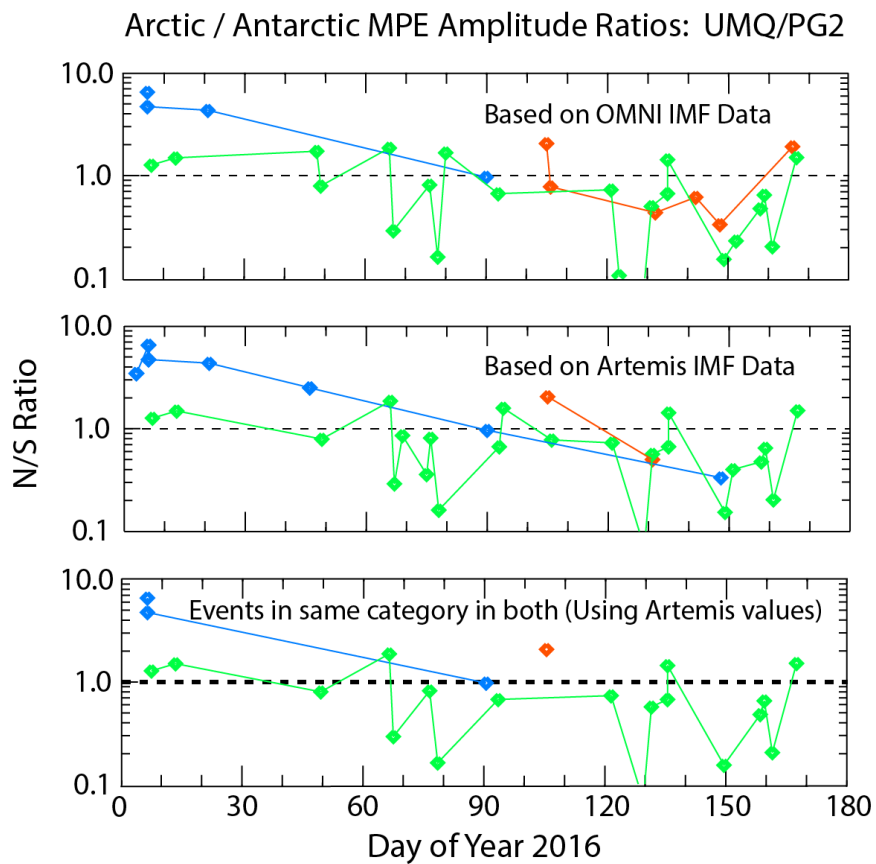


Figure S1. Plots of the ratios of amplitudes of MPE events observed at the UMQ/PG2 conjugate station pair as in Figure 8.

Arctic / Antarctic MPE Amplitude Ratios: GDH/PG3

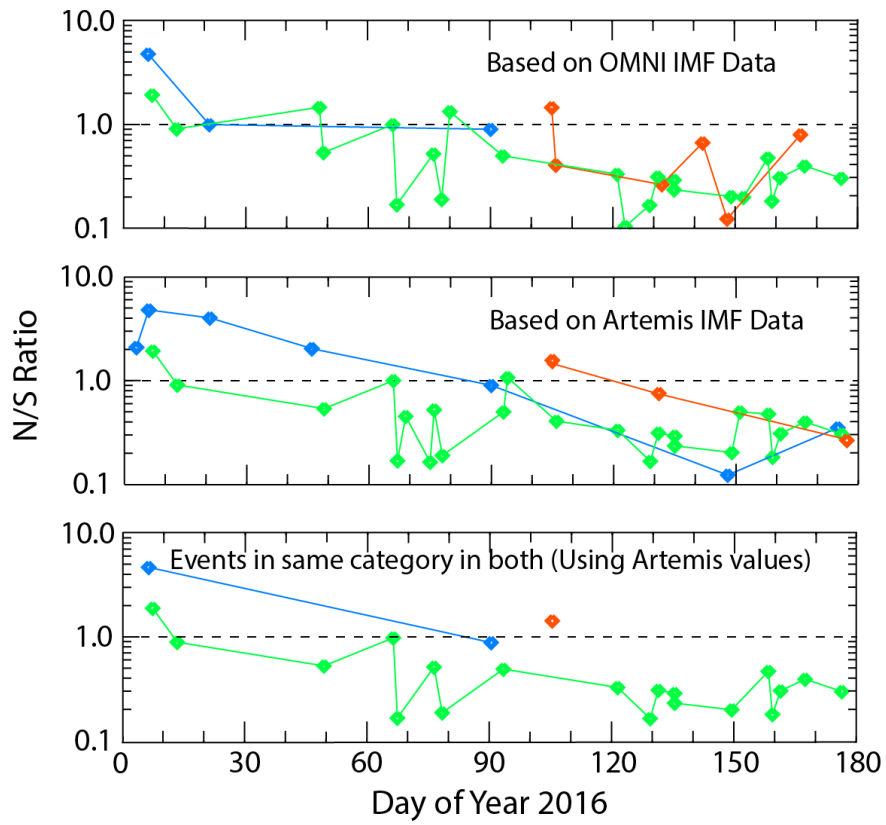


Figure S2. Plots of the ratios of amplitudes of MPE events observed at the GDH/PG3 conjugate station pair as in Figure 8.

Arctic / Antarctic MPE Amplitude Ratios: SKT/PG5

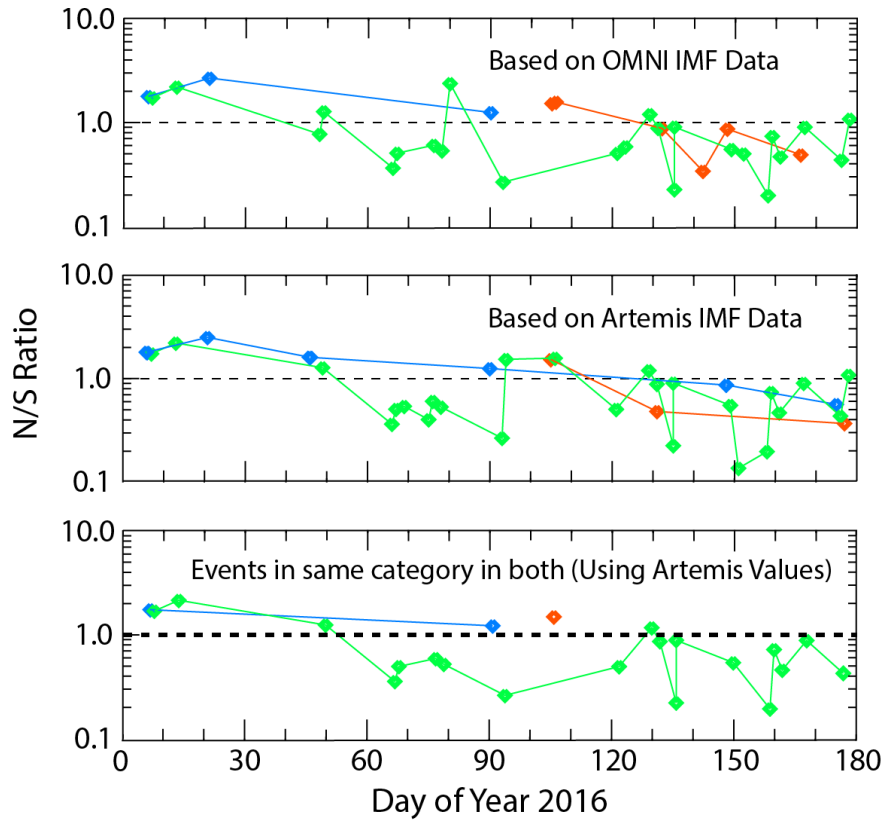


Figure S3. Plots of the ratios of amplitudes of MPE events observed at the SKT/PG5 conjugate station pair as in Figure 8.

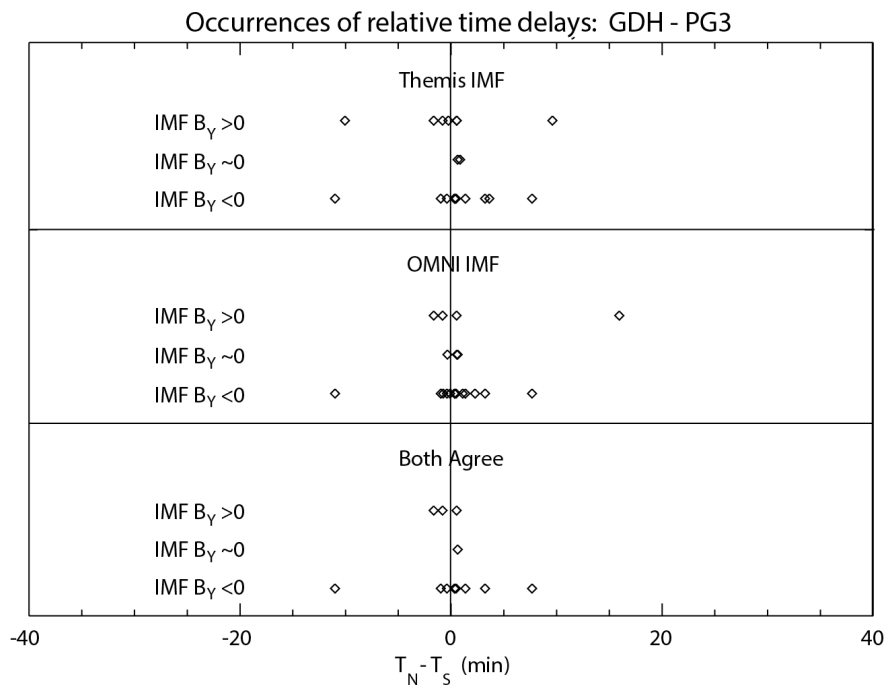


Figure S4. Plots of the distribution of time delays ($T_N - T_S$) between observations of the ΔBx minima associated with each MPE event in at the GDH – PG3 station pair as in Figure 9.

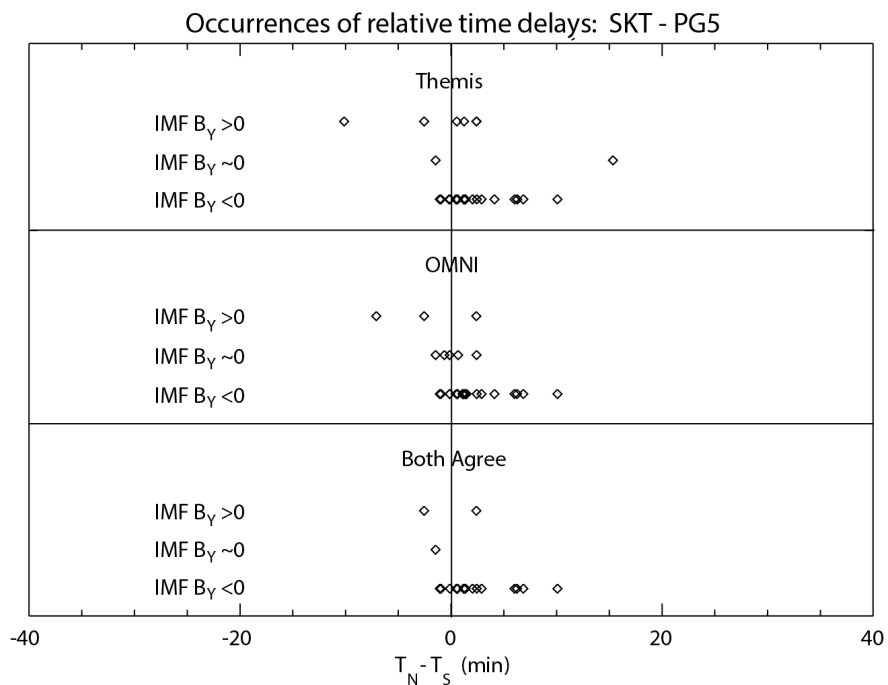


Figure S5. Plots of the distribution of time delays ($T_N - T_S$) between observations of the ΔBx minima associated with each MPE event in at the SKT – PG5 station pair as in Figure 9.

Hosted file

essoar.10511178.1.docx available at <https://authorea.com/users/524908/articles/595581-magnetic-perturbation-events-mpes-that-cause-gics-investigating-their-interhemispheric-conjugacy-and-control-by-imf-orientation>

Magnetic Perturbation Events (MPEs) that cause GICs:
Investigating their Interhemispheric Conjugacy and Control
by IMF Orientation

Mark J. Engebretson¹, Laura E. Simms^{1,2}, Viacheslav A. Pilipenko^{1,3}, Lilia Bouayed^{1,4}, Mark B. Moldwin², James M. Weygand⁵, Michael D. Hartinger⁶, Zhonghua Xu⁷, C. Robert Clauer⁷, Shane Coyle⁷, Anna N. Willer⁸, Mervyn P. Freeman⁹, and Andy J. Gerrard¹⁰

¹Department of Physics, Augsburg University, Minneapolis, MN

²Department of Climate and Space Sciences and Engineering, University of Michigan, Ann Arbor, MI

³Space Research Institute, Moscow, Russia

⁴Now at the Department of Physics, University of Minnesota, Minneapolis, MN

⁵Department of Earth, Planetary, and Space Sciences, University of California, Los Angeles, CA

⁶Space Science Institute, Boulder, CO

⁷Bradley Department of Electrical and Computer Engineering, Virginia Polytechnic Institute and State University, Blacksburg, VA

⁸DTU Space, Kongens Lyngby, Denmark

⁹British Antarctic Survey, Cambridge, UK

¹⁰Department of Physics, New Jersey Institute of Technology, Newark, NJ

submitted to the *Journal of Geophysical Research: Space Physics*

April 22, 2022

Key Words: magnetic perturbation events, geomagnetically induced currents, GIC, magnetic conjugacy, substorms, geomagnetic storms

Key Points:

Large (>6 nT/s) magnetic perturbation events (MPEs) were identified in data from conjugate magnetometer arrays in Greenland and Antarctica

MPE amplitudes were larger in the winter hemisphere and larger in the north (south) when IMF B_y was > 0 (< 0)

Minima in the Bx component of most MPEs appeared simultaneously (within 3 minutes) in conjugate hemispheres

Abstract

Nearly all studies of impulsive magnetic perturbation events (MPEs) that can produce dangerous geomagnetically induced currents (GICs) have used data from the northern hemisphere. In this study we investigated MPE occurrences during the first 6 months of 2016 at four magnetically conjugate high latitude station pairs using data from the Greenland West Coast magnetometer chain and from Antarctic stations in the conjugate AAL-PIP magnetometer chain. Events for statistical analysis and four case studies were selected from Greenland/AAL-PIP data by detecting the presence of >6 nT/s derivatives of any component of the magnetic field at any of the station pairs. For case studies, these chains were supplemented by data from the BAS-LPM chain in Antarctica as well as Pangnirtung and South Pole in order to extend longitudinal coverage to the west. Amplitude comparisons between hemispheres showed a) a seasonal dependence (larger in the winter hemisphere), and b) a dependence on the sign of the B_y component of the interplanetary magnetic field (IMF): MPEs were larger in the north (south) when IMF B_y was > 0 (< 0). A majority of events occurred nearly simultaneously (to within ± 3 min) independent of the sign of B_y as long as $B_y \geq 2 B_z$. As has been found in earlier studies, IMF B_z was < 0 prior to most events. When IMF data from Geotail, Themis-B, and/or Themis C in the near-Earth solar wind were used to supplement the time-shifted OMNI IMF data, the consistency of these IMF orientations was improved.

1. Introduction

This study continues our efforts to identify physical factors associated with magnetic perturbation events (MPEs) – solitary perturbations of 5-10 min duration and amplitudes of hundreds (or more) nT – that are known to be causally related to geomagnetically induced currents (GICs) that can damage power grids and pipeline systems as a result of their rapid changes of magnetic field. GICs are one of the many phenomena included in the field of space weather; extreme space weather events are now recognized as a serious threat to worldwide technological infrastructure (Boteler et al., 1998), and efforts to document, understand, and eventually predict them are under way in many nations around the world (e.g., Knipp and Gannon, 2019). Observations of the extreme geomagnetic storms of May 1921 and March 1989 and their effects, including large GICs, have been reported by Boteler (2019), Hapgood (2019), and Love et al. (2019). Knipp (2015) presented an annotated bibliography of studies of GICs, and Ngwira and Pulkkinen (2019) provided a list of recent studies of GIC events as part of a Geophysical monograph on GICs and their impacts on power systems (Gannon et al., eds., 2019).

Nearly all prior studies of magnetic perturbation events (MPEs) have used northern hemisphere data. This is especially appropriate at high latitudes: large populations in Northern Europe are affected by GICs, but there are no large populations at high latitudes in the southern hemisphere. However, because perturbations of the ionospheric plasma in the northern hemisphere depend in part on the ionospheric conductivity in both hemispheres and on the plasma/driving conditions along the entire length of magnetic field lines connecting them, in-

terhemispheric comparisons are needed to fully validate theories and models of MPEs, whether in the northern or southern hemisphere.

A set of four case studies by Engebretson et al. (2020) comparing MPEs observed in latitudinally extended magnetometer arrays at magnetically conjugate high latitude locations in the Arctic (Greenland and eastern Canada) and Antarctica found that these nighttime MPE events appeared within a few minutes of each other at stations in opposite hemispheres but with similar magnetic latitudes. These events occurred under a wide range of geomagnetic conditions, but common to each was a negative interplanetary magnetic field Bz that often exhibited at least a modest increase at or near the time of the event. This study also noted that the MPE amplitude was largest in the winter hemisphere during 3 of the 4 intervals presented, and concluded, using these data along with models of ionospheric conductances, that MPEs corresponded better to driving by a current generator model than by a voltage generator model. IMF orientations dominated by large By components are known to cause some nonconjugate magnetospheric and ionospheric effects at high latitudes, but the effect of IMF By on MPEs was not addressed in this earlier study.

In a more recent superposed epoch study Engebretson et al. (2021b) reported that the medians of nearly all the nearly 700 ~ 6 nT/s MPEs observed at 5 stations in Arctic Canada during 2015 and 2017, both premidnight and post-midnight, were preceded by intervals of negative IMF Bz . This pattern held for the 25th and 75th percentile traces in most cases as well, but not every Bz trace was negative prior to MPE occurrence or showed a similar time dependence. This paper also included work comparing a set of 156 intervals during 2015 compiled by Shane Coyle of Virginia Tech when the IMF vector was within $\pm 30^\circ$ of the GSM Y-axis, By was > 6 nT, and events lasted longer than 30 minutes, to the times of 200 MPE occurrences at 3 stations in eastern Arctic Canada during that year. Only one of these MPEs occurred during the time of a large IMF By event. These results suggested that conditions strongly dominated by IMF By orientations may suppress the magnetotail instabilities that appear to be the cause of these events, but did not address the effect of moderate or zero IMF By conditions on MPEs or their conjugacy. This current study was begun with the intent to look for the influence of IMF By and possibly other factors that might affect the interhemispheric conjugacy of these events, using all nighttime MPEs with amplitudes ~ 6 nT/s (~ 360 nT/min) that appeared in at least one station in magnetically conjugate subsets of these same Greenland and Antarctic arrays during the first six months of 2016.

In this study we present four case studies as well as detailed information on a large number of MPEs observed in conjugate hemispheres. We can confirm our earlier findings that IMF By polarity and seasonal effects cause hemispheric differences in amplitude, but even combined these are unable to account for the large variability in amplitude ratios, and we also demonstrate the near simultaneity of many of these events in both hemispheres. Section 2 describes the data used in this study and the procedures used to identify and quantify

conjugate events. Section 3 presents four multistation case studies, and section 4 presents statistical studies that focus on the relative amplitude and timing of these events. Section 5 discusses the implications of these observations, and Section 6 summarizes our findings.

2. Data Set and Analysis Methods

Northern hemisphere magnetometer data used in this study were recorded by the Greenland West Coast magnetometer chain (<https://www.space.dtu.dk/MagneticGroundStations>) and the MACCS array (<https://doi.org/10.48322/sydj-ab90>, Engebretson et al., 1995). Southern hemisphere data were recorded by the AAL-PIP magnetometer chain in Antarctica (Clauer et al., 2014), the British Antarctic Survey (BAS) Low Power Magnetometer chain (Kadokura et al., 2008), and the fluxgate magnetometer at South Pole Station, Antarctica (Lanzerotti et al., 1990; Engebretson et al., 1997). Data are presented in local magnetic coordinates. In the northern hemisphere (at MACCS, CANMOS and Greenland West Coastal chain stations) and in the southern hemisphere (at AAL-PIP and BAS LPM stations) the sensor axes are oriented as follows: X: magnetic north, Y: magnetic east, and Z: vertically down. The South Pole magnetometer sensors are X: magnetic north, Y: magnetic east, and Z: vertically upward (a left-handed system). The sampling rate of MACCS data is 2 Hz, and for the other stations 1 Hz.

Figure 1 and Table 1 show that South Pole Station in Antarctica is in approximate magnetic conjugacy to MACCS station Pangnirtung in Canada. Figure 1 also shows that the six AAL-PIP stations in Antarctica, located about 20° farther east in corrected geomagnetic (CGM) longitude, are in close magnetic conjugacy to the middle of the Greenland West Coast chain, and that the BAS LPM chain is conjugate in CGM magnetic latitude to several of the lower latitude Greenland West Coast stations, but approximately midway in CGM longitude between the Canadian and Greenland stations (Table 1).

The statistical part of this study is based on data from a subset of four stations in the equatorward part of the AAL-PIP array (PG2, PG3, PG4, and PG5) and four nearly conjugate stations ((UMQ, GDH, STF, and SKT respectively) in the Greenland West Coast Chain. Data from 2016 were chosen for study because of the best AAL-PIP up-time during conditions of either active or moderate solar activity. The limitation to the first six months is a consequence of the power availability at the remote AAL-PIP stations. These are powered by solar cells and batteries, and at most of these stations the batteries discharged slightly more than halfway through the calendar year. For case studies data from these stations were supplemented by data from Pangnirtung, South Pole, and the three most poleward stations of the BAS-LPM Chain (M85, M84, and M83) in order to provide a modest extension of longitudinal coverage to the west but in the same range of MLAT. The separation in MLT of SPA from GDH and of PGG from STF is ~ 1.3 hours, and PGG is at a predominantly westward distance of 673 km from STF.

Full-day data from each of the stations in the four Greenland/AAL-PIP station pairs were analyzed to identify MPEs with amplitude ≥ 6 nT/s each day at each station. Events were selected and derivatives calculated using the semi-automatic procedure described by Engebretson et al. (2019a). This procedure began by displaying a daily magnetogram (a 24-hour 3-axis plot of the magnetic field at each station) in local geomagnetic coordinates on a computer screen. Once a rapid (< 20 min duration) and large amplitude ($> \sim 200$ nT) magnetic perturbation was visually identified, the IDL cursor function was used to select times before and after the perturbation. The times and values of extrema in this interval were recorded for each component, and after application of a 10-point smoothing to reduce noise and eliminate isolated bad data points, the data were numerically differentiated using the 3-point Lagrangian approximation. Plots of the time series of data and derivatives were produced and saved, and the maximum and minimum derivative values were automatically determined and recorded.

Interplanetary magnetic field data for these studies were taken from three sources: a) the OMNI database accessed via CDAWEB (<https://cdaweb.gsfc.nasa.gov/index.html/>), which provides measurements from the L1 upstream libration point after time-shifting to the nose of the magnetosphere, b) observations by the Artemis spacecraft (Themis B and C) in orbit around the moon (also accessed via CDAWEB) and c) from the much nearer Geotail spacecraft, in orbit around the Earth (Weygand and McPherron, 2006a,b) and (<http://vmo.igpp.ucla.edu/data1/Weygand/PropagatedSolarWindGSM/weimer/Geotail/>). Only Artemis and Geotail data verified to be in the solar wind were retained.

3. Case Studies

For each of the events presented in this section we show a composite figure consisting of two-hour excerpts of 3-axis magnetograms (in local geomagnetic coordinates) from the stations listed above, as well as simultaneous two-hour plots of the IMF (in GSM coordinates) from the OMNI time-shifted database and a near-Earth monitor (either Geotail or Themis B). Also included at the bottom of each figure is a table listing the largest derivative (in any component, and either positive or negative) at each station during this interval, and an orange circle on the corresponding plot indicates the time of its occurrence. For each event we also note the timing of its occurrence relative to a recent geomagnetic storm (if any) and in Table 2 we list the most recent prior substorms (if any), as compiled in three substorm lists (Newell and Gjerloev, 2011, Forsyth et al., 2015, and Ohtani and Gjerloev, 2020) available on the SuperMAG web site (<https://supermag.jhuapl.edu/substorms/>).

Data obtained during the first event exhibited very similar magnetic perturbations and derivatives with comparable amplitudes in the northern and southern polar regions. During the second and third events much stronger perturbations and derivatives appeared in one hemisphere. The fourth event exhibited more complex patterns.

3.1. April 14, 2016

Figure 2 shows IMF and high latitude magnetometer data from 2000 to 2200 UT April 14, 2016, with the interval from 2040 to 2120 UT highlighted. Column (a) shows time-shifted IMF data in GSM coordinates from OMNI and Geotail, respectively. The three columns at the right show magnetic field components from (b) South Pole Station and BAS LPM stations M85, M84, and M83; (c) AAL-PIP stations PG2, PG3, PG4, and PG5; and (d) Greenland West Coast stations UMQ, GDH, STF, and SKT. Traces from these stations are arranged vertically in order of magnetic latitude. The vertical arrow in column (b) indicates that the Bx trace from M83 has been shifted to lower latitude to not overlap the M84 trace.

The initial negative turnings of the Bx component near 2043 UT were nearly simultaneous at the lowest latitude stations in both hemispheres in all three columns (b, c, and d). The Bx minima were strongest between 70 and 72° MLAT. Perturbations in By and Bz had opposite signs in the two hemispheres. As noted by Engebretson et al. (2020), the relative orientations of the Bx and By perturbations most likely reflect the hemispheric difference in the circular Hall current flow around a localized field-aligned current (FAC), counterclockwise in the Northern Hemisphere and clockwise in the Southern Hemisphere.

The largest ΔBx perturbations were similar and their minima occurred within ~3 minutes of each other near 2052 UT at latitudinally conjugate stations in Antarctica (PG4 and PG5) and Greenland (STF and SKT). They were smaller and occurred later at the higher latitude stations (PG2, PG3, UMQ and GDH). These differences show both the localized nature of the MPEs and the often-observed poleward motion of the structures that generate these events, as noted earlier in case studies presented by Engebretson et al. (2019b). In addition, although there was a general similarity between the amplitudes of ΔBx and of the derivatives, they were not strictly proportional. This lack of proportionality in amplitude has been noted in several earlier studies as well (Viljanen 1997, Viljanen et al. 2006; and Engebretson et al. 2019a). It can also be seen that the largest derivatives appeared on the slopes of the ΔBx perturbations, not at their minima, and thus did not occur at the same time. Similar or slightly weaker ΔBx perturbations appeared at corresponding times at the BAS LPM stations to the west.

This event occurred at the end of the main phase of a geomagnetic storm (minimum SYM/H = -67 nT). The solar wind velocity (V_{sw}) was ~ 410 km/s, the solar wind dynamic pressure (P_{sw}) was ~ 2.2 nPa, and the AL and AU magnetic indices (replace by SML, SMU?) were ~ -500 nT and ~ 250 nT, respectively. Three prior substorm onsets between 2020 and 2030 UT were identified on this day (Table 2), but none of them appeared in all three substorm lists, and it is not clear that the MPE onset near 2050 UT was closely related to any of them. (It is important to note that the Ohtani and Gjerloev (2020) list only includes isolated substorms.)

In the OMNI data shown in panel a1, IMF B_z rose from -3 nT to -2 nT coincident with the beginning of the MPE at 2050 UT and returned to -5 nT at 2055 UT. In the near-Earth Geotail data shown in panel a, B_z rose more gradually from -3 nT to -1 nT during the interval before returning to -3 nT after 2050 UT. In both OMNI and Geotail data the B_y component fell gradually until ~2051 UT, shortly before the time of MPE onset, and then rose rapidly past 0 near 2055 UT.

Figure 3 shows equivalent ionospheric currents produced using the Spherical Elementary Current Systems (SECS) method (Weygand et al., 2009, 2011) for both the northern and southern hemispheres at two times: at 2015 UT during the geomagnetically quiet period before the MPE (panels a and b), and at 2052 UT, during the time of the strongest magnetic perturbations at the lower latitude stations (panels c and d). The left (right) panels displays the northern (southern) hemisphere currents plotted over the landmasses (gray curve) in a magnetic coordinate system with magnetic noon at the top, dawn on the right side, dusk on the left side, and magnetic midnight at the bottom. The dots mark where the equivalent current has been derived and the vector indicates the magnitude and direction of the current. The stars indicate stations with good data for this date. The amplitude key for the currents is in the lower right corner of each panel.

In panel a) a portion of the dusk side convection cell is apparent and the throat of the cusp starts just north of the Northwest Territories. The eastward electrojet crosses over Hudson Bay and the east coast of Canada. Panel b) shows the equivalent ionospheric currents in the southern hemisphere over a limited region. The southern hemisphere is shown as a glass earth projection so magnetic noon at the top, dawn on the right side, dusk on the left side, and magnetic midnight at the bottom. Because of the limited magnetometer coverage in Antarctica only a small portion of the eastward electrojet is visible near Coats Land, Antarctica. Panels c) and d) display the equivalent ionospheric currents during the MPE event. In general, in the Northern hemisphere all the currents are significantly larger, the duskside convection cell is still present, and the throat of the cusp is not readily apparent most likely because IMF B_y is about -3 nT. The MPE is visible in the lower latitude portion of Greenland around magnetometer stations STF and SKT as equivalent ionospheric currents pointing toward the sun. The MPE is also apparent in Antarctica near stations PG4 and PG5 as equivalent ionospheric currents pointing toward the sun.

The SECS technique also identified pairs of upward and downward currents (a proxy for FACs) in both hemispheres. An upward current appeared south of STF and a downward current north of it (not shown). Similarly, an upward current appeared south of PG3 and PG4 and a downward current north of these stations. Applying the right hand rule to the Pedersen current connecting the two vertical current pairs reproduces the westward equivalent current seen in panels c) and d). However, because of the paucity of magnetometer coverage east and west of these arrays, we cannot determine the longitudinal extent of

the inferred FACs or the location of their epicenters.

3.2. January 6, 2016

Figure 4 shows IMF and high latitude magnetometer data from 0000 to 0200 UT January 6, 2016 with the interval between 0030 and 0130 UT highlighted. This geomagnetically quiet interval ($Dst = +12$) occurred 6 days after the most recent geomagnetic storm. The solar wind velocity (V_{sw}) was ~ 500 km/s, the solar wind dynamic pressure (P_{sw}) was ~ 5.52 nPa, and the AL and AU magnetic indices (replace by SML, SMU?) were ~ -700 nT and ~ 100 nT, respectively. Several substorm onsets (Table 2) were noted prior to or during this interval (very differently in the 3 lists), but only the one at 0057 UT appeared to closely precede the MPEs.

Sharp drops in B_x appeared near 0037 UT at STF and SKT in Greenland, simultaneous with weak inflections at PG4 in Antarctica, the more poleward Greenland stations GDH and UMQ, and PGG in Arctic Canada. Sharp drops at these four latter stations appeared near 0057 UT. Short-lived transient perturbations can be seen to occur within the subsequent negative bays at each of these stations, culminating in final large spikes near 0125 UT, but perturbations were larger in all 3 components at all northern hemisphere stations than at southern hemisphere stations at comparable latitudes. Perturbations farther west, at PGG, appeared to be intermediate in amplitude but slightly delayed in time relative to those at comparable latitudes in Greenland. In contrast, variations at SPA, PG2, and PG3 during this interval were very weak. Perturbations in B_x at Antarctic stations at lower latitude (M85, M84, M83, and PG4) were similar to but weaker than those at STF and SKT, and their perturbations in the B_y and B_z components were again significantly weaker.

Both the OMNI and Geotail data showed that during the highlighted interval the IMF B_z component was again mostly negative but that the IMF B_y component was positive. The B_y magnitude was larger than the B_z magnitude in OMNI data but similar in Geotail data.

3.3. March 6, 2016

Figure 5 shows IMF and high latitude magnetometer data from 2130 to 2330 UT March 6, 2016 with the interval between 2200 and 2245 UT highlighted. This interval coincided with the end of the main phase of a strong geomagnetic storm ($Dst = -98$ nT). The solar wind velocity (V_{sw}) was ~ 500 km, the solar wind dynamic pressure (P_{sw}) was ~ 8 nPa, and the AL and AU magnetic indices (replace by SML, SMU?) were ~ -700 nT and ~ 150 nT, respectively. Several substorm onsets were noted prior to or during this interval (very differently in the 3 lists); the onset at 2158 occurred just before the beginning of the highlighted interval, but none of the onsets occurred within the interval.

Only very small perturbations and derivatives appeared at the higher latitude Antarctic stations SPA, PG2, and PG3 and at the higher latitude Greenland stations PGG, UMQ, and GDH, consistent with a storm-induced equatorward

expansion of the auroral oval. Large perturbations and derivatives appeared at Antarctic stations M85, M84, M83, PG4 and PG5, but only much smaller perturbations and derivatives appeared at Greenland stations STF and SKT. We also note that the B_x minima at PG4 and STF occurred nearly simultaneously.

Both the OMNI and Themis B data showed that during the highlighted interval the IMF B_y component was strongly negative (near -10 nT). The IMF B_z component in Themis B data was negative but relatively steady and smaller, near -7 nT, and the OMNI B_z component was near -7 nT between 2248 and 2235 but slightly positive before and after that interval. During this event Themis B was located upstream and on the dawnside of Earth, at $R_x = 49 R_E$, $R_y = -27 R_E$, and $R_z = 3 R_E$ in GSE coordinates. Geotail was in the magnetosphere during this interval.

3.4. May 11, 2016

Figure 6 shows IMF and high latitude magnetometer data from 0000 to 0200 UT May 11, 2016 with two short intervals highlighted: 0040 to 0105 UT and 0110 to 0120 UT. This moderately disturbed interval ($Dst = -28$) occurred on the 4th day of recovery after a strong geomagnetic storm with minimum $Dst = -88$. The solar wind velocity (V_{sw}) was ~ 550 km/s, the solar wind dynamic pressure (P_{sw}) was ~ 0.8 nPa, and the AL and AU magnetic indices (replace by SML, SMU?) were ~ -250 nT and ~ 140 nT, respectively. Table 2 shows that two substorm onsets occurred during the final hour of the previous day (May 10), and one onset (included only in the Forsyth et al. list) occurred at 0058 UT.

There was considerable magnetic activity throughout this two-hour period, but it was generally weaker than in the three previous examples (note the smaller scale of the vertical axis during this event). During the first highlighted interval large magnetic bays appeared at the lower latitude Antarctic stations M85, M84, M83, PG3, PG4, and PG5, with narrow spikes in several components at 0100 UT at M83 (9.8 nT), PG4 (5.8 nT), and PG5 (5.8 nT). Much weaker bays and spikes appeared at SPA and PG2, and very little activity appeared at UMQ and GDH. Slightly stronger variations appeared at STF and SKT, with a narrow spike only in the B_z component at SKT (4.6 nT). During the second highlighted interval negative bays were evident only at SPA and more weakly at PGG, but large derivatives appeared at many stations that showed little evidence of negative bays. Large narrow spikes with large derivatives appeared in all three components at 0115 UT at STF (8.0 nT) and SKT (5.1 nT), and much smaller peaks appeared in B_z at UMQ and GDH. Spikes of moderate to large derivative amplitude also appeared simultaneously at 0115 UT in one or more components at PG3 (5.3 nT), PG4 (3.7 nT), and PG5 (3.0 nT), and in the higher latitude range to the west in both hemispheres, at SPA (5.6 nT), PGG (5.0 nT), and M85 (2.0 nT).

IMF data from OMNI, Geotail, and Themis B (not shown) were not only variable but showed significant disagreement during this two-hour interval, as were

also the data from the three L1 monitors (not shown). In particular, during the first shaded interval the Bz component observed by OMNI was > 0 between 0040 and 0054 UT before dropping to ~ -1 nT at 0100 UT, while the Bz component observed by Geotail was negative throughout. The By component in OMNI data was near 0 until 0100 UT, while the By component in Geotail data was near 1 nT until 0105 UT. During the second interval the observed Bz traces varied in opposite directions. The Bz component in OMNI data was near -1 nT at 0110 UT, but rose to near 0 after 0114 UT. The Bz component in Geotail data was near +0.3 nT at the beginning of this interval and dropped to negative values (~ -1 nT) after 0115 UT. The By components in OMNI and Geotail data remained mostly negative during this second interval, but again varied in opposite directions.

Note especially the isolated spike at many stations near 0116 UT that was nearly simultaneous at many stations both N and S. It was not associated with any significant magnetic bay at most stations, so was presumably caused by a very localized set of ionospheric and/or field-aligned currents.

Table 3 summarizes the characteristics of the case study events, including the occurrence of nearly simultaneous conjugate ΔBx minima. The variety in IMF By polarity and geomagnetic activity will be considered in the next section.

4. Statistical Studies

A total of 66 separate >6 nT/s MPEs were identified at one or more of the stations in the four Greenland-Antarctica station pairs listed above during the first 6 months of 2016. A large majority of these exceeded 6 nT/s at one or both stations in more than one station pair. In the few cases during which more than one > 6 nT/s MPE was identified at a given station during a given 2 h UT interval, only the largest amplitude event was counted.

Columns 2 and 4 of Table 4 list the number of MPEs with derivatives > 6 nT/s in any component at the northern and southern hemisphere station in each station pair, respectively. Columns 6-10 show the number of events at each station pair with 1 or 2 exceeding the 6 nT/s threshold, and their sum and ratio, respectively. It is clear that more > 6 nT/s events appeared at the two lower latitude station pairs (45 and 55) than at the two higher latitude pairs (19 and 34). This latitudinal pattern is similar that found in Table 2 of Engebretson et al. (2021a) for stations at comparable magnetic latitudes in eastern Arctic Canada.

4.1 Seasonal Trend

Figure 7 shows the ratio of derivatives at northern and southern stations, $dB_N/dt / dB_S/dt$, for each of the four conjugate station pairs as a function of the day of the year in 2016. Each panel shows only those events with at least one > 6 nT/s event at each station pair. A linear fit to the base 10 logarithm of the ratios as a function of day of the year is also shown. There is considerable scatter in each plot, but the lines fit the distributions reasonably well (there is

little evidence for a nonlinear relation). These panels clearly show a seasonal dependence on the slope; it is roughly twice as steep for the highest latitude UMQ/PG2 pair as for the lower latitude STF/PG4 and SKT/PG5 pairs.

4.2. IMF B_y Dependence

In an attempt to identify a source for the scatter in each of the amplitude ratio plots in Figure 7, we next examined the IMF B_z and B_y components (using both OMNI and Artemis/Themis time-shifted IMF data as available) to determine their values prior and up to the time of MPE occurrences. Of the 66 MPEs, 47 (71%) were preceded by an interval of at least 15 minutes of IMF $B_z < 0$, while 5 were preceded by IMF $B_z > 0$, and another 14 by intervals with mixed IMF B_z polarity. However, only 34 of the 47 MPEs with consistently negative IMF B_z values had a consistent IMF B_y value (+, within 1 nT of 0, or -) during this same interval. Figure 8 shows the MPE amplitude ratios for the STF/PG4 station pair following these intervals of consistently negative IMF B_z and consistent IMF B_y values. Events with $B_y > 1$ nT are shown in blue, B_y within 1 nT of 0 in red, and $B_y < -1$ in green. Panels a) and b) show all events for which OMNI data and Artemis/Themis IMF data satisfied these conditions, respectively, and panel c) shows only those events for which OMNI and Artemis/Themis data both saw consistent IMF $B_z < 0$ and the same category of consistent IMF B_y values. Plots for the other station pairs are shown as Figures S1-S3 in the supporting information. The patterns shown are consistent with a small IMF B_y effect (N/S ratio larger for $B_y > 1$, than for $B_y < -1$) that is convolved with a seasonal effect, but there is considerable overlap, and the numbers of $B_y > 1$ and B_y near 0 events are very small.

Table 5 shows the results of an ANCOVA (analysis of covariance) test of the difference between the means of the $B_y > 1$ and $B_y < -1$ MPE amplitude ratio distributions for each of the four station pairs after removal of the linear fits to a seasonal trend using the linear fits shown in Figure 7. The few $B_y \sim 0$ events were not included in this analysis. Mean differences were calculated for the mean date of observations at each station. The differences in the means were statistically significant for all four station pairs based on OMNI data, for the three of the station pairs based on Artemis/Themis data, and for both combined data sets (all 4 station pairs). Although both a seasonal variation and a dependence on the sign of IMF B_y are evident in Figures 7 and 8 and the IMF B_y effect is statistically significant, even together they are not sufficient to explain much of the scatter in amplitude ratios.

4.3. Time delay analysis

The addition of stations somewhat west of the Greenland - AAL-PIP conjugate arrays in the case studies above gave little direct evidence for any IMF B_y -induced longitudinal skewing in opposite hemispheres. It also became apparent while surveying all the MPEs in this data set that in many cases the waveforms of the B_x (north-south) component at conjugate stations were roughly simultaneous (the two minima occurred within 3 minutes of each other). Events

with such near simultaneity were also noted in Figures 2, 5, and 6. In order to further investigate the conditions leading to close timing between conjugate hemispheres, we determined the time of each ΔBx minimum to within ± 1 second by successively zooming in on magnetograms of each of the MPE events at each station in the three lowest latitude station pairs.

Figure 9 shows the distribution of time delays (positive values are associated with later event times in the north than in the south) for the STF – PG4 station pair. The relative timing error is ± 2 seconds, much less than the size of the diamond symbols. What stands out in all 3 sets is that there are two populations: one with $T_N - T_S < 3$ min, and the other with larger time differences, ranging from ~ 5 to ~ 30 min. All nine distributions in Figure 9 are dominated by events with time delays clustered within 3 min of 0, but also show a small number of events with much larger delays. In each of the three panels IMF $By > 1$ events are skewed slightly to the left and IMF $By < -1$ events are skewed to the right. In the bottom panel, however, using only those events for which Themis and OMNI IMF observations agreed, the pattern was more consistent: $By > 0$ to the left, $By \sim 0$ near 0, and $By < 0$ to the right with only one exception. Figures for the GDH – PG3 and SKT – PG5 station pairs showing similar distributions are shown as Figures S4 and S5 in the supporting information.

Figure 10 provides a comparison of the distributions from all three of these station pairs, but combines events in all three IMF By categories in one histogram. Events were strongly peaked near 0 at each station pair and in both data sets, but with a slight skewing toward more positive values in the OMNI data compared to the Artemis/Themis data. The few large time lags in either direction occurred most often in the STF – PG4 data set.

In order to better characterize the dependence of $T_N - T_S$ on the IMF By/Bz ratio, Figure 11 shows a plot of time differences $T_N - T_S$ as a function of the IMF By/Bz ratio component in Artemis/Themis data for all events where the signs of the IMF Bz and By components in the Artemis and OMNI data bases agreed. In addition, only events with a fairly steady By/Bz ratio during the 15 minutes prior to the MPE were included in these plots. This resulted in a further reduction in the number of events and reduced even further the number of events with $By > 0$. Because of the small number of events, this plot includes all events at three conjugate station pairs (GDH-PG3, STF-PG4, and SKT-PG5). Table 6 provides information on the number of events at each of the three station pairs, indicating that for 77% of these events the Bx minima occurred within 3 minutes of each other.

The accuracy of the times of Bx minima at each station, determined from high resolution plots with a range of 1 min, was usually $< \pm 1$ s. The accuracy of each $T_N - T_S$ value is thus usually ± 2 s, a value much smaller than the plot symbols. Errors in IMF By and Bz were derived from visual estimates of half the distance from the mean to either approximate extreme during the 15 min prior to the MPE. The extremes of these values were then used to calculate the errors in the IMF By/Bz ratio. The resulting error limits ranged from ± 0.3 to

± 1.5 .

The division into two populations noted above is evident in Figure 11: most have time delays between -3 and +3 minutes, and a much smaller number have delays from 3 to 15 min. There is no evident dependence on the B_y/B_z ratio for the events between -3 and +3 minutes; the events in this population have a remarkably flat distribution. It is also evident that most of the events in Figure 11 are in the left half. This again reflects the strong skewing of all large MPE events in this data set to be associated with intervals of negative IMF B_y . Although the distribution of events with time delays above 3 min in Figure 9 are skewed slightly to the left for $B_y > 1$ events and to the right for $B_y < -1$ events, and Figure 11 gives evidence of a relation between the polarity of the IMF B_y component and the relative time delay between northern and southern conjugate stations, their number is so small and the IMF ratio errors so large that any slope determined from these data is not statistically significant. We also looked for a seasonal trend in the time delays, but no pattern was evident for either extreme or modest time differences.

5. Discussion

This paper has compared observations of large magnetic perturbation events at high northern and southern latitudes to better understand their similarities and differences at magnetically conjugate high latitude sites. We have identified a clear seasonal variation and a somewhat weaker dependence on the sign of the B_y component of the IMF, using data from the OMNI data base (using data from the L1 upstream libration point that has been time-shifted to the nose of the magnetosphere), from the Artemis/Themis spacecraft (in orbit about the Moon, again after time-shifting), and from the Geotail spacecraft (in orbit about Earth). None of these three provided usable data for all the events cataloged during the first 6 months of 2016, and in a considerable number of cases the available data exhibited at least minor differences.

The May 11, 2016 event is one of several exceptions to the general pattern of N/S derivative amplitude ratio depending on the sign of IMF B_y . Given the observed amplitudes of perturbations in the two shaded intervals, one might expect either small or negative IMF B_y at 0100 UT and either small or positive IMF B_y at 0115, along with a negative IMF B_z . It is possible that neither IMF data set correctly shows the IMF data that impinged on the magnetosphere during this interval.

Determining the character of the IMF that actually impinges on Earth's magnetosphere presents many challenges, as noted by Weimer et al. (2002), Borovsky (2018) and Burkholder et al. (2020) and exemplified in a study of Pc 3-4 waves by Bier et al. (2014). In both our case studies and statistical studies we have presented data using IMF data from both OMNI and a nearer-Earth monitor. These have produced modest but recognizable differences in the resulting patterns in amplitudes, but have led to similar general conclusions regarding the influence of seasonal and IMF B_y effects on the ratios of amplitudes at conju-

gate stations. Even in combination these influences are insufficient to remove most of the scatter in these ratios. A check of the values of the IMF magnitude and solar wind velocity and pressure for each event revealed no additional external pattern of influence that would explain the remaining scatter in conjugate amplitudes.

5.1. Amplitude Comparisons

The control of MPE amplitude by IMF B_y reported here is consistent with the results of several earlier studies. Holappa et al. (2021a) noted that many studies using ground magnetometers, beginning with Friis-Christensen et al. (1975) and using polar-orbiting satellites (Friis-Christensen et al., 2017 and Smith et al., 2017), have shown that auroral electrojets in the northern hemisphere winter are stronger in both hemispheres for $B_y > 0$ than for $B_y < 0$, and that In NH summer the dependence on the B_y sign is reversed. Holappa et al. (2021a) noted that this B_y sign dependence is very strong in the winter hemisphere, but it is weak in the summer hemisphere, and is much stronger in the westward electrojet than in the eastward electrojet.

In addition, Workayehu et al. (2021), using nearly 6 years of magnetic field measurements from the Swarm A and C satellites, reported that auroral currents were stronger in the northern hemisphere than the southern hemisphere for IMF $B_y > 0$ in most local seasons under both signs of IMF B_z . This pattern provides an explanation for the distribution of IMF orientations in the ecliptic plane shown in the Engebretson et al. (2021b) superposed epoch study of MPEs observed in Arctic Canada, because the northern hemisphere values would be stronger for $B_y > 0$, so more likely to exceed the 6 nT/s amplitude threshold. The distributions of IMF B_x and B_y , shown separately in Figure 9 of that paper, included both positive and negative values, but the median in B_x was < 0 and that in B_y was > 0 , consistent with a Parker-spiral oriented IMF vector directed toward Earth. Figure S7 in the Supporting Information of that paper, showing the medians of the x - y vector component of the IMF, revealed that a Parker-Spiral vector directed Earthward (with $B_y > 0$) was observed consistently for premidnight events occurring less than 30 min after the most recent substorm onset (panels a1-a5), and was often observed also during most premidnight events occurring between 30 and 60 min after substorm onset (panels b1-b5). However, the directions and sign of the B_y component were much more varied and at times had ortho-Parker-Spiral orientation for postmidnight events. (It is notable that no postmidnight MPEs during the first half of 2016 satisfied the selection criteria for the present study.)

Our observations of a strong seasonal dependence regardless of the sign of IMF B_y appear to be somewhat inconsistent with the IMF B_y polarity dependence in these earlier studies. However, Workayehu et al. (2021) also reported a complex dependence on season, and it is conceivable that the seasonal dependence evident in our data set might be restricted to the longitude region and/or 6 month period where these observations were made.

A subsequent study by Holappa et al. (2021b) found that the substorm onset latitude and the isotropic boundary latitude of energetic protons were both $\sim 1^\circ$ lower during IMF $B_y > 3$ conditions than for smaller B_y , and that the substorm occurrence frequency was larger for small B_y . They suggested, consistent with the results of a resistive MHD study by Hesse and Birn et al. (1990), that the magnetotail was more stable during conditions of large IMF B_y , requiring the magnetotail lobes and the polar cap to contain more flux to initiate a substorm compared to the situation when B_y was small. Our observations that MPEs were strongly suppressed under IMF conditions dominated by the B_y component (Engebretson et al., 2021b) and occurred only when preceded by intervals of IMF $B_z < 0$ and conditions when IMF $B_y < 2$ IMF B_z (this study) suggests that their generation is in some way linked to magnetotail reconnection.

A possible explanation for the remaining scatter in amplitude ratios that is independent of seasonal or IMF B_y -related factors is based on the horizontal dimensions of the MPEs and of the effective separation (from ~ 150 to ~ 300 km) and range of sensitivity of ground-based magnetometers. Belakhovsky et al. (2018), using data from the IMAGE magnetometer network, reported that magnetic field variations associated with GICs had a spatial scale of a few hundred km, consistent with estimates of the horizontal half-amplitude radius of the MPEs reported by Engebretson et al. (2019a,b) of ~ 275 km, and by Weygand et al. (2021) of ~ 250 - 450 km, with a somewhat greater longitudinal extent in some cases. The sensitivity of a ground magnetometer to ionospheric currents varies as the inverse square of the distance from the magnetometer on the ground to the current in the overhead ionosphere (~ 100 to 150 km altitude), and thus also falls off rapidly as the horizontal separation exceeds 200 - 300 km. If the center of an event fell within 200 - 300 km of both the northern and southern “conjugate” stations, both stations would see the same event with little additional difference in amplitude. If the horizontal distance between the center of an MPE and only one ground magnetometer site exceeded 200 - 300 km, this would produce an additional reduction in the measured amplitude at that station.

5.2. Relative Timing

We have also noted that MPEs observed in conjugate hemispheres very often occurred nearly simultaneously (within < 3 min) regardless of IMF B_y polarity as long as $B_y < \sim 2B_z$. Many satellite imaging studies reviewed by Ohma et al. (2018) using simultaneous observations of similar auroral features in both hemispheres have shown that they are displaced longitudinally when IMF $B_y \neq 0$, such that when IMF $B_y > 0$ structures appear in the southern auroral zone up to ~ 2 hours MLT later than in the north (i.e., shifted eastward), and vice versa for IMF $B_y < 0$. Østgaard et al. (2011b), using data from several years of conjugate auroral observations from the IMAGE and Polar spacecraft, found a sinusoidally varying mean longitudinal displacement at substorm onset between the two hemispheres that maximized near ± 0.5 h MLT at IMF clock angles of 90° and 270° , respectively, and an event study by Reistad et al. (2016) showed displacements of up to 3 h MLT.

However, substorms have been observed to rapidly decrease this displacement. Østgaard et al. (2011a) found that the conjugate auroral features became more similar in MLT during the expansion phase of two substorms. Throughout the first substorm the IMF was stable and B_y dominated, so they concluded that the longitudinal displacement was removed by processes related to the magnetospheric substorm. Ohma et al. (2018) subsequently presented 10 case studies confirming that a reduction in the longitudinal displacement was a common signature of substorms: the aurora became more north-south symmetric in 8 to 30 min, which is similar to the typical duration of the substorm expansion phase, and the rate of change was related to the reconnection rate.

As noted in earlier studies by Engebretson et al. (2021a,b), the majority of >6 nT/s MPEs most often occurred within 30 minutes after substorm onsets (but only very rarely coinciding with them), although many others occurred long after the onset of any prior substorm. If MPEs are triggered by reconnection in the magnetotail, as appears likely, then this close agreement in Bx minima associated with MPEs should also be expected for events occurring shortly after a substorm onset, as happened prior to all four of the case study events presented above, but a time shift should be expected for events occurring after extended intervals of lesser geomagnetic activity.

The ten events shown in Figure 11 with $T_n - T_s > 3$ min (appearing earlier in the north) were all associated with IMF $B_y < 0$. This is consistent with the shift in auroral longitudes observed by Østgaard et al. (2011a) and Ohma et al. (2018). The values of the AL index one hour before the occurrence of the MPEs shown in Figure 11 provide additional evidence suggesting consistency with their findings. The values of the AL index one hour before the ten MPE events with $T_n - T_s > 3$ ranged from -10 to -350 nT, with a mean of -117 nT and a median of -105 nT, characteristic of relatively quiet conditions. In contrast, the AL values during the 33 events with $T_n - T_s < 3$ min ranged from -40 to -460 nT, with a mean of -191 nT and a median of -180 nT, indicating somewhat more disturbed conditions.

The relative timing pattern noted here is also subject to observational uncertainties, however. The magnetic conjugacy between locations in Antarctica and Greenland is known to vary with season and dipole tilt as well as with magnetic activity, which in turn is parameterized in empirical magnetic field models by magnetic indices and the components of the IMF. According to their nominal corrected geomagnetic latitudes, GHB (69.2°) is slightly closer to the conjugate latitude of PG5 (-69.9°) than is SKT (70.7°) and SKT is slightly closer to the conjugate latitude of PG4 (-71.2°) than is STF (71.9°). Using the T89 model to trace the field lines of the West Greenland stations to the surface of Antarctica, at 2100 UT on April 14 2016 (using $K_p = 3.333$) SKT was magnetically very close to PG5 and PG4 was at the same magnetic latitude as STF but shifted westward, consistent with the pairing used to determine amplitude ratios above. However, at 0100 UT on May 11 2016 (using $K_p = 2.0$), GHB was magnetically very close to PG5 and SKT was very close to PG4. Given these K_p values,

higher latitude stations were near or outside the region of closed field lines, so no conjugate tracing using the T89 model was possible.

Motivated by the variation in conjugacy indicated by these model results, we have calculated the timing differences between the MPE Bx minima for the GHB-PG5 and SKT-PG4 station pairs in order to compare them with SKT-PG5 and STF-PG4 station pairs. Table 7 shows the number of events with the differences between Bx minima > 3 and < 3 min for each of these pairs, using all 66 events regardless of IMF conditions but excluding those events at which multiple closely spaced minima appeared at one or both stations. The number of events in the GHB-PG5 column was reduced because no data were available from GHB between May 22 and June 2.

Table 7 shows that the number of Bx minima simultaneous to within 3 min was more than double the number with larger time delays for three of the four station pairs. The numbers for GHB-PG5 were almost equal, and the reason for this discrepancy is not clear. These comparisons suggest that despite the modest shifts in conjugacy expected between hemispheres at these high magnetic latitudes, the similarities and differences reported in section 4 above appear to be reasonably consistent.

6. Conclusions

Using the only currently available conjugate high latitude magnetometer arrays, we have investigated the conjugacy of large transient magnetic perturbation events that, if they occurred over more technologically developed regions, would generate large GICs. Four case studies have demonstrated some of the similarities and differences between MPE events in conjugate hemispheres, and by using 6 months of magnetic field data from four conjugate station pairs in West Greenland and Antarctica in combination with measurements of the IMF, we have been able to quantify their dependence on season and IMF B_z and B_y polarity. Uncertainty in the IMF dependences stems from the still-limited number of events, the high variability of the IMF, and disagreements between currently available sources of IMF data due to the lack of consistent measurements near the Earth-Sun line and near Earth. In addition, some of the variability in the timing of conjugate MPEs may be due to the inaccuracy and variability of conjugate mappings between hemispheres.

1. We have found that IMF B_z was < 0 shortly during the 15 minutes preceding and/or during a large majority (71%) of these events (as in our other recent studies). This suggests but cannot strongly confirm the influence of reconnection in the magnetotail as a link in the causal chain leading to these events.
2. Two factors appeared to exert modest control over the relative amplitude of MPEs in the northern and Southern polar regions.
 - a) The N/S amplitude ratio was increased when IMF $B_y > 0$, and decreased when IMF $B_y < 0$.

1. Latitudinal/seasonal dependences caused MPEs to have larger amplitudes in the winter hemisphere.

The remaining differences in amplitude may be due at least in part to the convolution of the spatial localization of the ionospheric currents that cause these events and the horizontal range of detection of these currents by ground-based magnetometers.

1. The relative timing between conjugate MPEs (the majority of them simultaneous to within ± 3 min) was consistent both with the sense of longitudinal shift in auroral features revealed in earlier studies of simultaneous satellite images (Figure 9), and with the rapid reduction in these shifts during substorms. The addition of stations somewhat west of the West Greenland - AAL-PIP conjugate arrays in the case studies gave no evidence for any IMF B_y -induced longitudinal skewing in opposite hemispheres, consistent with the close temporal connection of many of these events to prior substorm activity.
2. MPEs were observed in conjugate hemispheres regardless of IMF B_y polarity as long as $B_y < \sim 2B_z$. As noted by Engebretson et al. (2021b), a separate study of 156 intervals in 2015 when the IMF was dominated by large B_y values found that only one of these coincided with an MPE in the northern hemisphere. This suggests that MPE occurrences are suppressed by large and dominant IMF B_y values.

Much work remains to be done before the dependences on external factors identified here can be accurately characterized. The statistical associations found here between MPE occurrences and prior intervals of IMF $B_z < 0$ and IMF B_y of either sign are insufficient to quantify any possible IMF-related delay time until MPE onset, in part because of the limitations of the IMF data bases themselves. In addition, the physical processes leading to MPEs are still only poorly understood. The fact that they occur not only during geomagnetically disturbed conditions but also during relatively quiet times suggests that although they are likely to be caused by instabilities in the magnetotail, ground-satellite conjunction studies at various tailward distances appear to necessary in order to characterize, and even more so to predict, the occurrence of the mesoscale or small-scale events that trigger them.

Data Availability Statement

OMNI Solar wind and IMF data are available at the Goddard Space Flight Center Space Physics Data Facility at <https://cdaweb.sci.gsfc.nasa.gov/index.html/>, as are also IMF data from the Artemis/Themis spacecraft and from the Greenland West Coast magnetometer chain. AAL-PIP magnetometer data are available in CDF and IDL save set formats at <http://mist.nianet.org/> and in ASCII format at <https://cdaweb.gsfc.nasa.gov>. MACCS magnetometer data are available in IAGA 2002 ASCII format at <http://space.augsburg.edu/maccs/requestdatafile.jsp> and in ASCII format at <https://cdaweb.gsfc.nasa.gov>. South Pole Station magnetometer data are available in ASCII format at <https://antarcticgeospace.njit.edu/Data/>,

and BAS LPM magnetometer data are available at <https://data.bas.ac.uk/full-record.php?id¼GB/NERC/BAS/AEDC/00263>). Geotail propagated data are available at (<http://vmo.igpp.ucla.edu/data1/Weygand/PropagatedSolarWindGSM/weimer/Geotail/>).

Acknowledgments

This research was supported by NSF grant AGS-2013648 to Augsburg University, AGS-2013433 to the University of Michigan, PLR-1543364, OPP-1744828, AGS-2027210, and AGS-2027168 to Virginia Tech, Natural Environment Research Council Grant NE/R016038/1 to the British Antarctic Survey, and OPP-1643700 to the New Jersey Institute of Technology. The spherical elementary currents produced by James M. Weygand were made possible by NASA grants 80NSSC18K1220, 80NSSC18K1227, 80NSSC20K1364, 80NSSC18K0570, NASA Contract 80GSFC17C0018, and NSF GEO-NERC 2027190.

Author Contributions

Conceptualization: Mark J. Engebretson, Michael D. Hartinger

Data curation: Anna N. Willer, Michael D. Hartinger, C. Robert Clauer, Mark J. Engebretson, Mark B. Moldwin, Mervyn P. Freeman, Andy J. Gerrard

Formal Analysis: Mark J. Engebretson, James M. Weygand, Laura E. Simms, S. Coyle, Viacheslav A. Pilipenko

Funding Acquisition: Mark J. Engebretson

Investigation: Mark J. Engebretson, Lilia Bouayed, James M. Weygand, Zhonghua Xu

Methodology: Mark J. Engebretson, James M. Weygand, Michael D. Hartinger

References

Belakhovsky, V. B., Sakharov, Y. A., Pilipenko, V. A., & Selivanov, V. N. (2018). Characteristics of the

variability of a geomagnetic field for studying the impact of the magnetic storms and substorms

on electrical energy systems, *Izvestiya. Physics of the Solid Earth*, *54*, 52–65.

<https://doi.org/10.1134/S1069351318010032>

Bier, E. A., Owusu, N., Engebretson, M. J., Posch, J. L., Lessard, M. R., and Pilipenko, V. A. (2014).

Investigating the IMF cone angle control of Pc3-4 pulsations observed on the ground. *Journal of Geophysical Research: Space Physics*, *119*, 1797–1813. <http://doi.org/10.1002/2013JA019637>

Borovsky, J. E. (2018). The spatial structure of the oncoming solar wind at Earth and the shortcomings

of a solar-wind monitor at L1. *Journal of Atmospheric and Solar–Terrestrial Physics*, 177, 2–11.

<http://doi.org/10.1016/j.jastp.2017.03.014>

Boteler, D. H. (2019). A 21st century view of the March 1989 magnetic storm. *Space Weather*, 17,

1427–1441. <https://doi.org/10.1029/2019SW002278>

Boteler, D. H., Pirjola, R. J., & Nevanlinna, H. (1998). The effects of geomagnetic disturbances on

electrical systems at the Earth’s surface. *Advances in Space Research*, 22, 17–27. [https://doi.org/10.1016/S0273-1177\(97\)01096-X](https://doi.org/10.1016/S0273-1177(97)01096-X)

Burkholder, B. L., Nykyri, K., & Ma, X. (2020). Use of the L1 Constellation as a Multispacecraft Solar

Wind Monitor. *Journal of Geophysical Research: Space Physics*, 125, e2020JA027978.

<https://doi.org/10.1029/2020JA027978>

Clauer, C. R., Kim, H., Deshpande, K., Xu, Z., Weimer, D., Musko, S., et al. (2014). An autonomous

adaptive low-power instrument platform (AAL-PIP) for remote high-latitude geospace data

collection. *Geoscientific Instrumentation, Methods and Data Systems*, 3, 211–227.

<https://doi.org/10.5194/gi-3-211-2014>

Engebretson, M. J., Araki, T., Arnoldy, R. L., Carpenter, D. L., Doolittle, J. H., Fukunishi, H., et al. (1997).

The United States automatic geophysical observatory (AGO) program in Antarctica. In M.

Lockwood, M. N. Wild, & H. J. Opgenoorth (Eds.), *The satellite-ground based coordination*

sourcebook, ESA-SP-1198 (pp. 65–99). ESTEC, Noordwijk, Netherlands: ESA Publications.

Engebretson, M. J., W. J. Hughes, J. L. Alford, E. Zesta, L. J. Cahill, Jr., R. L. Arnoldy, and G. D. Reeves

(1995). Magnetometer array for cusp and cleft studies observations of the spatial extent of

broadband ULF magnetic pulsations at cusp/cleft latitudes, *Journal of Geophysical Research*,

100, 19371-19386, <https://doi.org/10.1029/95JA00768>

Engebretson, M. J., Pilipenko, V. A., Ahmed, L. Y., Posch, J. L., Steinmetz, E. S., Moldwin, M. B., Connors,

M. G., Weygand, J. M., Mann, I. R., Boteler, D. H., Russell, C. T., and Vorobev, A. V. (2019a). Nighttime magnetic perturbation events observed in Arctic Canada: 1. Survey and statistical analysis. *Journal of Geophysical Research: Space Physics*, *124*, 7442-7458. <https://doi.org/10.1029/2019JA026794>

Engebretson, M. J., Steinmetz, E. S., Posch, J. L., Pilipenko, V. A., Moldwin, M. B., Connors, M. G.,

Boteler, D. H., Mann, I. R., Hartinger, M. D., Weygand, J. M., Lyons, L. R., Nishimura, Y., Singer,

H. J., Ohtani, S., Russell, C. T., Fazakerley, A., & Kistler, L. M. (2019b). Nighttime magnetic

perturbation events observed in Arctic Canada: 2. Multiple-instrument observations. *Journal*

of Geophysical Research: Space Physics, *124*, 7459-7476. <https://doi.org/10.1029/2019JA026797>

Engebretson, M. J., K. R. Kirkevold, E. S. Steinmetz, V. A. Pilipenko, M. B. Moldwin, B. A. McCuen, C. R.

Clauer, M. D. Hartinger, S. Coyle, H. Opgenoorth, A. Schillings, A. N. Willer, T. R. Edwards, D. H. Boteler, A. J. Gerrard, M. P. Freeman, and M. C. Rose (2020), Interhemispheric Comparisons of Large Nighttime Magnetic Perturbation Events Relevant to GICs, *Journal of Geophysical Research: Space Physics*, *125*, e2020JA028128. <https://doi.org/10.1029/2020JA028128>

Engebretson, M. J., V. A. Pilipenko, E. S. Steinmetz, M. B. Moldwin, M. G. Connors, D. H. Boteler, H. J.

Singer, H. Opgenoorth, A. Schillings, S. Ohtani, J. Gjerloev, and C. T. Russell (2021a). Nighttime magnetic perturbation events observed in Arctic Canada: 3. Occurrence and amplitude as functions of magnetic latitude, local time, and magnetic disturbances. *Space Weather*, *19*, e2020SW002526. <https://doi.org/10.1029/2020SW002526>

Engebretson, M. J., L. Y. Ahmed, V. A. Pilipenko, E. S. Steinmetz, M. B. Moldwin, M. G. Connors, D. H.

Boteler, J. M. Weygand, S. Coyle, S. Ohtani, J. Gjerloev, and C. T. Russell (2021b). Superposed

- epoch analysis of nighttime magnetic perturbation events observed in Arctic Canada (2021), *Journal of Geophysical Research: Space Physics*, 126, e2021JA029465. <https://doi.org/10.1029/2021JA029465>.
- Forsyth, C., Rae, I. J., Coxon, J. C., Freeman, M. P., Jackman, C. M., Gjerloev, J., & Fazakerley, A. N. (2015). A new technique for determining Substorm Onsets and Phases from Indices of the Electrojet (SOPHIE). *J. Geophys. Res. Space Physics*, 120, 10,592–10,606. <https://doi.org/10.1002/2015JA021343>
- Friis-Christensen, E., Finlay, C. C., Hesse, M., & Laundal, K. M. (2017). Magnetic field perturbations from currents in the dark polar regions during quiet geomagnetic conditions. *Space Science Reviews*, 206 (1–4), 281–297. <https://doi.org/10.1007/s11214-017-0332-1>
- Friis-Christensen, E., & Wilhelm, J. (1975). Polar cap currents for different directions of the interplanetary magnetic field in the Y-Z plane. *Journal of Geophysical Research*, 80(10), 1248–1260. <https://doi.org/10.1029/JA080i010p01248>
- Gannon, J. L., A. Swidinsky, A., & Xu, Z. (Eds.) (2019), Geomagnetically induced currents from the Sun to the power grid, geophysical monograph series (Vol. 244). Washington, D.C., American Geophysical Union. <https://doi.org/10.1002/9781119434412>
- Hapgood, M. (2019). The great storm of May 1921: An exemplar of a dangerous space weather event. *Space Weather*, 17, 950–975. <https://doi.org/10.1029/2019SW002195>
- Hesse, M. & Birn, J. (1990). Magnetic reconnection in the magnetotail current sheet for varying cross-tail magnetic field. *Geophysical Research Letters*, 17(11), 2019–2022. <https://doi.org/10.1029/gl017i011p02019>
- Holappa, L., Robinson, R. M., Pulkkinen, A., Asikainen, T., & Mursula, K. (2021a). Explicit IMF *By*-dependence in geomagnetic activity: Quantifying ionospheric electrodynamics. *Journal of Geophysical Research: Space Physics*, 126, e2021JA029202. <https://doi.org/10.1029/2021JA029202>
- Holappa, L., Reistad, J. P., Ohma, A., Gabrielse, C., & Sur, D. (2021b). The magnitude of IMF *By*

influences the magnetotail response to solar wind forcing. *Journal of Geophysical Research: Space Physics*, 126, e2021JA029752. <https://doi.org/10.1029/2021JA029752>

Kadokura, A., Yamagishi, H., Sato, N., Nakano, K., & Rose, M. C. (2008). Unmanned magnetometer

network observation in the 44th Japanese Antarctic Research Expedition: Initial results and an

event study on auroral substorm evolution. *Polar Science*, 2, 223–235.

<https://doi.org/10.1016/j.polar.2008.04.002>

Knipp, D. J. (2015). Synthesis of geomagnetically induced currents: Commentary and research. *Space*

Weather, 13, 727–729. <https://doi.org/10.1002/2015SW001317>

Knipp, D. J., & Gannon, J. L. (2019). The 2019 National Space Weather strategy and action plan and

beyond. *Space Weather*, 17, 794–795. <https://doi.org/10.1029/2019SW002254>

Lanzerotti, L. J., Wolfe, A., Trivedi, N., MacLennan, C. G., & Medford, L. V. (1990). Magnetic impulse

events at high latitudes: Magnetopause and boundary layer plasma processes. *Journal of*

Geophysical Research, 95, 97–107. <https://doi.org/10.1029/JA095iA01p00097>

Love, J. J., Hayakawa, H., & Cliver, E. W. (2019). Intensity and impact of the New York Railroad

superstorm of May 1921. *Space Weather*, 17, 1281–1292. <https://doi.org/10.1029/2019SW002250>

Newell, P. T., & Gjerloev, J. W. (2011). Evaluation of SuperMAG auroral electrojet indices as indicators

of substorms and auroral power. *Journal of Geophysical Research*, 116, A12211. <https://doi.org/10.1029/2011JA016779>

Ngwira, C. M., & Pulkkinen, A. A. (2019). An introduction to geomagnetically induced currents (2019).

In J. L. Gannon, A. Swidinsky, & Z. Xu (Eds.), *Geomagnetically induced currents from the Sun to the power grid*, geophysical monograph series (Vol. 244, pp. 3–13). American Geophysical Union. <https://doi.org/10.1002/9781119434412.ch1>

Ohma, A., Østgaard, N., Reistad, J. P., Tenfjord, P., Laundal, K. M., Snekvik, K., et al. (2018). Evolution of

- asymmetrically displaced footpoints during substorms. *Journal of Geophysical Research: Space Physics*, *123*, 10,030–10,063. <https://doi.org/10.1029/2018JA025869>
- Ohtani, S., & Gjerloev, J. W. (2020). Is the substorm current wedge an ensemble of wedgelets?: Revisit to midlatitude positive bays. *Journal of Geophysical Research: Space Physics*, *125*, e2020JA027902. <https://doi.org/10.1029/2020JA027902>
- Østgaard, N., Humberstet, B. K., & Laundal, K. M. (2011a). Evolution of auroral asymmetries in the conjugate hemispheres during two substorms. *Geophysical Research Letters*, *38*, L03101. <https://doi.org/10.1029/2010GL046057>
- Østgaard, N., Laundal, K. M., Juusola, L., Åsnes, A., Haaland, S. E., & Weygand, J. M. (2011b). Interhemispherical asymmetry of substorm onset locations and the interplanetary magnetic field. *Geophysical Research Letters*, *38*, L08104. <https://doi.org/10.1029/2011GL046767>
- Reistad, J. P., Østgaard, N., Tenfjord, P., Laundal, K. M., Snekvik, K., Haaland, S. E., et al. (2016). Dynamic effects of restoring footpoint symmetry on closed magnetic field lines. *Journal of Geophysical Research: Space Physics*, *121*, 3963–3977. <https://doi.org/10.1002/2015JA022058>
- Viljanen, A. (1997). The relation between geomagnetic variations and their time derivatives and implications for estimation of induction risks. *Geophysical Research Letters*, *24*, 631–634. <https://doi.org/10.1029/97GL00538>
- Viljanen, A., Tanskanen, E. I., & Pulkkinen, A. (2006). Relation between substorm characteristics and rapid temporal variations of the ground magnetic field. *Annales Geophysicae*, *24*, 725–733. <https://doi.org/10.5194/angeo-24-725-2006>
- Weimer, D.R., Ober, D.M., Maynard, N. C., Burke, W. J., Collier, M. R., McComas, D. J., Ness, N. F., & C. W. (2002), *Journal of Geophysical Research: Space Physics*, *107*, 1210. <https://doi.org/10.1029/2001JA009102>
- Weygand, J. M., and McPherron, R. L. (2006a). Geotail Low Energy Particle (LEP) experiment data
- Weimer Propagated 60 s Resolution in GSM Coordinates, <https://doi.org/10.21978/P89S5D>

Weygand, J. M., and McPherron, R. L. (2006b). Geotail Weimer Propagated using CPI 60 s Resolution Tri-axial Fluxgate Magnetometer in GSM Coordinates, <https://doi.org/10.21978/P8SS5R>

Weygand, J. M. (2009). Equivalent Ionospheric Currents (EICs) derived using the Spherical Elementary Current Systems (SECS) technique at 10 s Resolution in Geographic Coordinates. University of California. <https://doi.org/10.21978/P8D62B>

Weygand, J. M., Amm, O., Viljanen, A., Angelopoulos, V., Murr, D., Engebretson, M. J., et al. (2011). Application and validation of the spherical elementary currents systems technique for deriving ionospheric equivalent currents with the North American and Greenland ground magnetometer arrays. *Journal of Geophysical Research*, 116, A03305. <https://doi.org/10.1029/2010JA016177>

Weygand, J. M., Engebretson, M. J., Pilipenko, V. A., Steinmetz, E. S., Moldwin, M. B., Connors, M. G., Nishimura, Y., Lyons, L. R., Russell, C. T., Ohtani, S., and Gjerloev, J. (2021). SECS analysis of nighttime magnetic perturbation events observed in Arctic Canada. *Journal of Geophysical Research: Space Physics*, 126, e2021JA029839. <https://doi:10.1029/2021JA029839>

Workayehu, A. B., Vanhamäki, H., Aikio, A. T., and Shepherd, S. G. (2021). Effect of interplanetary magnetic field on hemispheric asymmetry in ionospheric horizontal and field-aligned currents during different seasons. *Journal of Geophysical Research: Space Physics*, 126, e2021JA029475. <https://doi.org/10.1029/2021JA029475>

Table 1. Magnetometer Stations Used in this Study

Northern Hemisphere		Southern Hemisphere							
Array	Geogr Lat	Geogr Lon	CGM Lat	CGM Lon	Array	Geogr Lat	Geogr Lon	CGM Lat	CGM Lon
MACCS									
Pangnirtung	66.1°	294.2°	73.2°	19.8°	South Pole	-90.00 °	--	-74.5°	18.7
AAL-PIP									

Greenland Coastal Chain PG0 -83.67° 88.68° -78.7° 38.2°
 THL 77.47° 290.77° 84.0° 26.4° PG1 -84.50° 77.20° -77.3° 37.3°
 TAB 76.54° 291.18° 83.2° 25.0° PG2 -84.42° 57.95° -75.7° 39.1°
 SVS 76.02° 294.90° 82.3° 30.4° PG3 -84.81° 37.63° -73.9° 36.7°
 KUV 74.57° 302.82° 80.0° 39.4° PG4 -83.34° 12.25° -71.2° 36.4°
 UPN 72.78° 303.85° 78.2° 38.1° PG5 -81.96° 5.71° -69.9° 37.2°
 UMQ 70.68° 307.87° 75.7° 40.8°
 GDH 69.25° 306.47° 74.5° 37.8° British Antarctic Survey Low Power Magnetometer Chain
 ATU 67.93° 306.43° 73.2° 36.8° M85-002 -85.36° 2.06° -71.8° 30.1°
 STF 67.02° 309.28° 71.9° 39.5° M84-336 -84.36° -23.85° -69.8° 25.9°
 SKT 65.42° 307.10° 70.7° 36.1° M83-348 -82.90° -12.25° -69.2° 30.6°
 GHB 64.17° 308.27° 69.2° 36.8° M81-338 -80.89° -22.25° -67.0° 29.2°
 FHB 62.00° 310.32° 66.6° 38.1° M79-336 -79.68° -24.12° -66.0° 29.3°
 NAQ 61.16° 314.56° 65.0° 42.3° M78-337 -77.52° -23.42° -64.3° 30.7°

Note: Corrected geomagnetic (CGM) coordinates were calculated for epoch 2016 (using http://sdnet.thayer.dartmouth.edu/aacgm/aacgm_calc.php#AACGM).

Table 2. The universal times of substorm onsets identified within 2 hours prior to or during the four case studies presented in section 3. Times in parentheses are from the previous day. N & G 2011: Newell and Gjerloev, (2011) F 2015: Forsyth et al. (2015), O & G 2020: Ohtani and Gjerloev (2020)

Date	UT	YRDAY	N & G 2011	F 2015	O & G 2020
April 14, 2016	2100	16105	1912, 1957, 2022, 2043	1957, 2029	none
January 6, 2016	0100	16006	0032, 0057	0002	(2347)
March 6, 2016	2230	16066	2124, 2158	2125	none
May 11, 2016	0100	16132	none	(2304), 0058	(2326)

Table 3. Summary of the 4 case study events.

Date	Storm	Recent	Prior	AL	AU	IMF	Amplitude	Close	ΔB_x
Phase	Substorms	<i>B_y</i>	Ratio	Timing					

Apr. 14 End of Main Y 500, 250 nT ~0 N ~ S Y
 Jan. 6 Recov. Day 6 Y 700, 100 nT +6 nT N » S ?

Mar. 6 End of Main Y 770, 150 nT -10 nT S > N Y

May 11 Recov. Day 4 Y 250, 140 nT mixed mixed Y

Table 4. Number of > 6 nT/s MPEs recorded at four stations each in the Greenland West Coast Magnetometer Chain and in the AAL-PIP Magnetometer Chain.

Station	Events	Station	Events	Station Pair	Events > 6 nt/s per Pair	Ratio
Greenland	>6 nT/s	Antarctica	>6 nT/s	1 per pair	2 (both)	Total 2 ev/1 ev
UMQ	11	PG2	11	UMQ-PG2	16	3 19 0.19
GDH	18	PG3	23	GDH-PG3	27	7 34 0.26
STF	24	PG4	34	STF-PG4	32	13 45 0.41
SKT	29	PG5	42	SKT-PG5	39	16 55 0.41

Table 5. ANCOVA test of the difference between the means of the $B_y > 0$ and $B_y < 0$ MPE amplitude ratios for each of the four station pairs after removal of the effects of the linear seasonal variations.

	OMNI	Artemis
Station pair	Avg diff at mean yrday	Avg diff at mean yrday
UMQ/PG2	2.536* \pm 1.163	1.724* \pm 0.937
GDH/PG3	1.644* \pm 0.960	1.298* \pm 0.664
STF/PG4	1.066* \pm 0.717	0.985* \pm 0.643
SKT/PG5	0.696* \pm 0.628	0.373a \pm 0.44
All stn pairs	1.588* \pm 0.465	1.126* \pm 0.338

* statistically significant (p-value < 0.05)

a: not statistically significant (p-value = .094)

Table 6. The number MPEs with time differences between Bx minima of < 3 and > 3 min, respectively, for three Arctic-Antarctic station pairs. Events were restricted to those for which the IMF had a fairly steady B_y/B_z ratio in Artemis/Themis data during the 15 minutes prior to the MPE and the Artemis/Themis and OMNI data agreed on their signs.

Δt	GDH-PG3	STF-PG4	SKT-PG5	Total	Total %
$\Delta t < 3$	7	13	13	33	77
$\Delta t > 3$	2	4	4	10	23
Total Events	9	17	17	43	100

Table 7. The number MPEs with time differences between Bx minima < 3 and > 3 min, respectively, for four Arctic-Antarctic station pairs. Events with isolated minima are included here regardless of IMF orientations.

Tdiff SKT-PG5 GHB-PG5 STF-PG4 SKT-PG4

$\Delta t < 3$ 41 21 35 38

$\Delta t > 3$ 14 20 17 18

Total Events 55 41 52 56

Figures

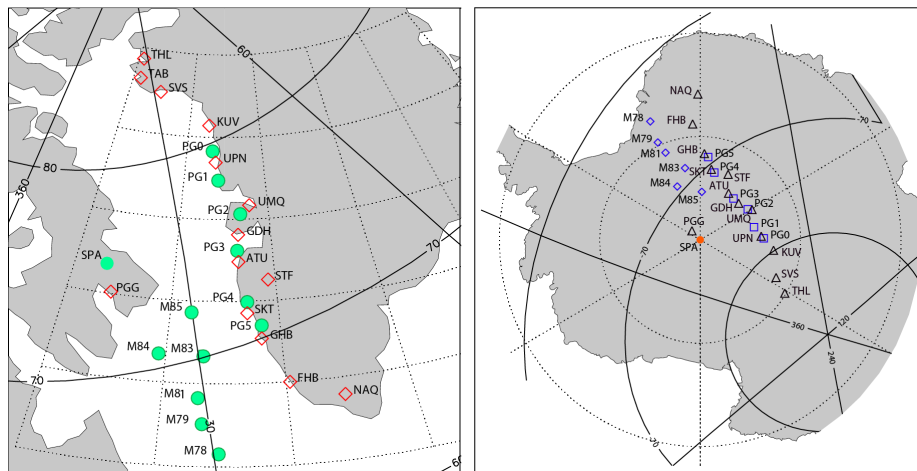


Figure 1. Maps showing the location of ground magnetometer stations used for this study. a) Map of Arctic Canada and Greenland, showing stations in the northern hemisphere (red diamonds) and the conjugate mapped locations of southern hemisphere stations (green circles). b) Map of Antarctica, showing stations in the southern hemisphere (diamonds, squares, and red circle) and the conjugate mapped locations of northern hemisphere stations (triangles). Solid lines show corrected geomagnetic coordinates. Conjugate mappings were based on the IGRF model magnetic field for epoch 2016 (<https://omniweb.gsfc.nasa.gov/vitmo/cgm.html>)

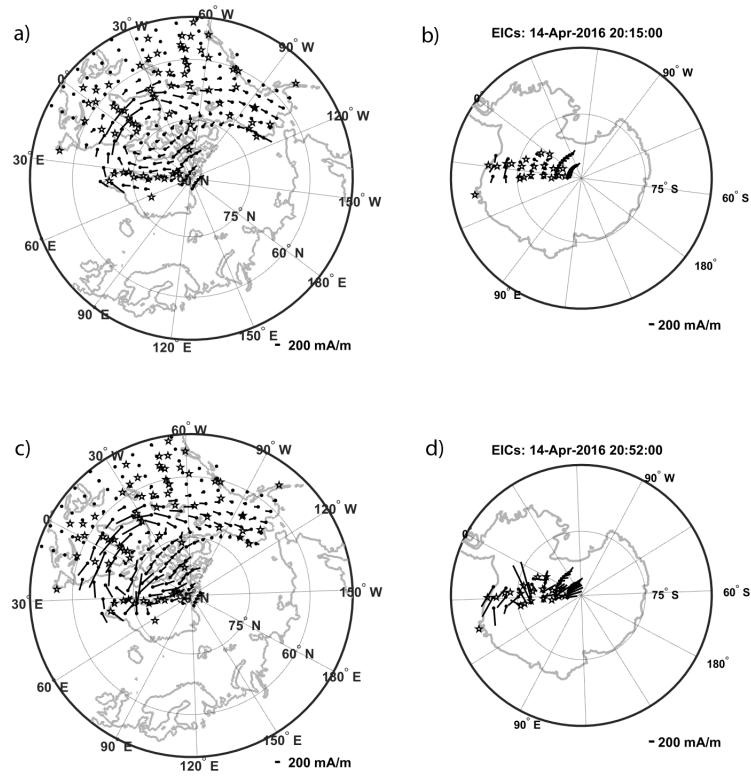
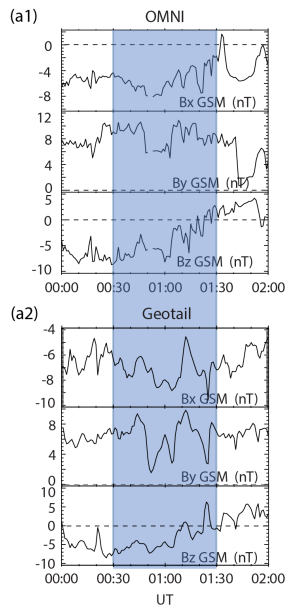


Figure 3. Equivalent ionospheric currents produced using the Spherical Elementary Current Systems method for both the northern and southern hemispheres at two times: at 2015 UT (panels a and b) and 2052 UT (panels c and d). The left (right) panels display the northern (southern) hemisphere currents plotted over the landmasses (gray curve) in a magnetic coordinate system with magnetic noon at the top, dusk on the left side, and magnetic midnight at the bottom.

January 6, 2016

YRDAY = 16006



Peak Derivatives (nT/s)					
SPA	1.8	PG2	1.4	UMQ	9.1
PGG	9.6	PG3	2.3	GDH	11.0
M85	3.7	PG4	4.2	STF	8.1
M84	4.5	PG5	no data	SKT	10.1
M83	3.5				

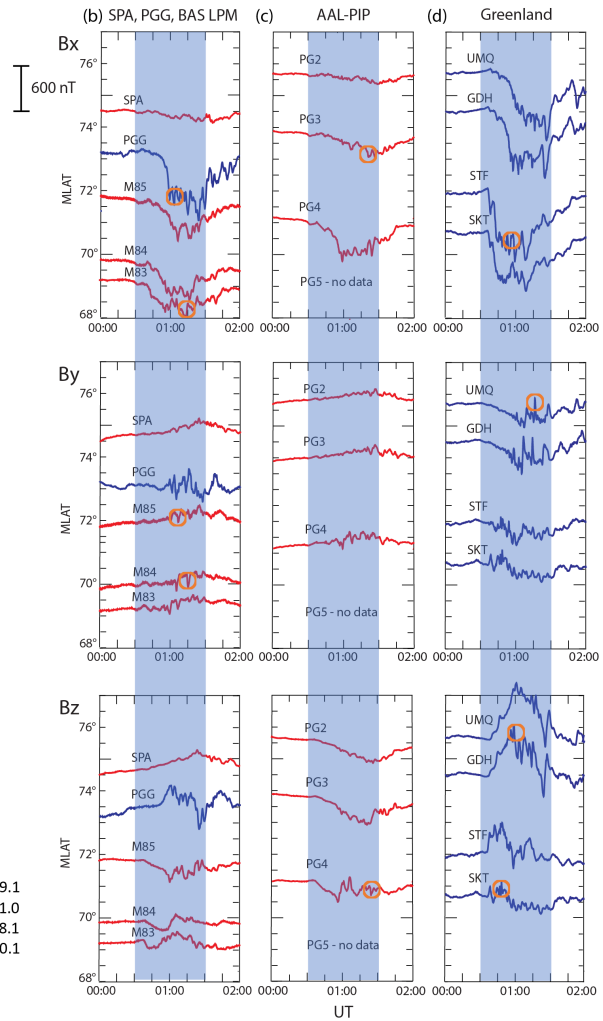


Figure 4. Composite figure showing IMF and high latitude magnetometer data from 0000 to 0200 UT January 6, 2016, as in Figure 2. A small orange circle is located near the largest derivative (if > 2 nT/s) at each station.

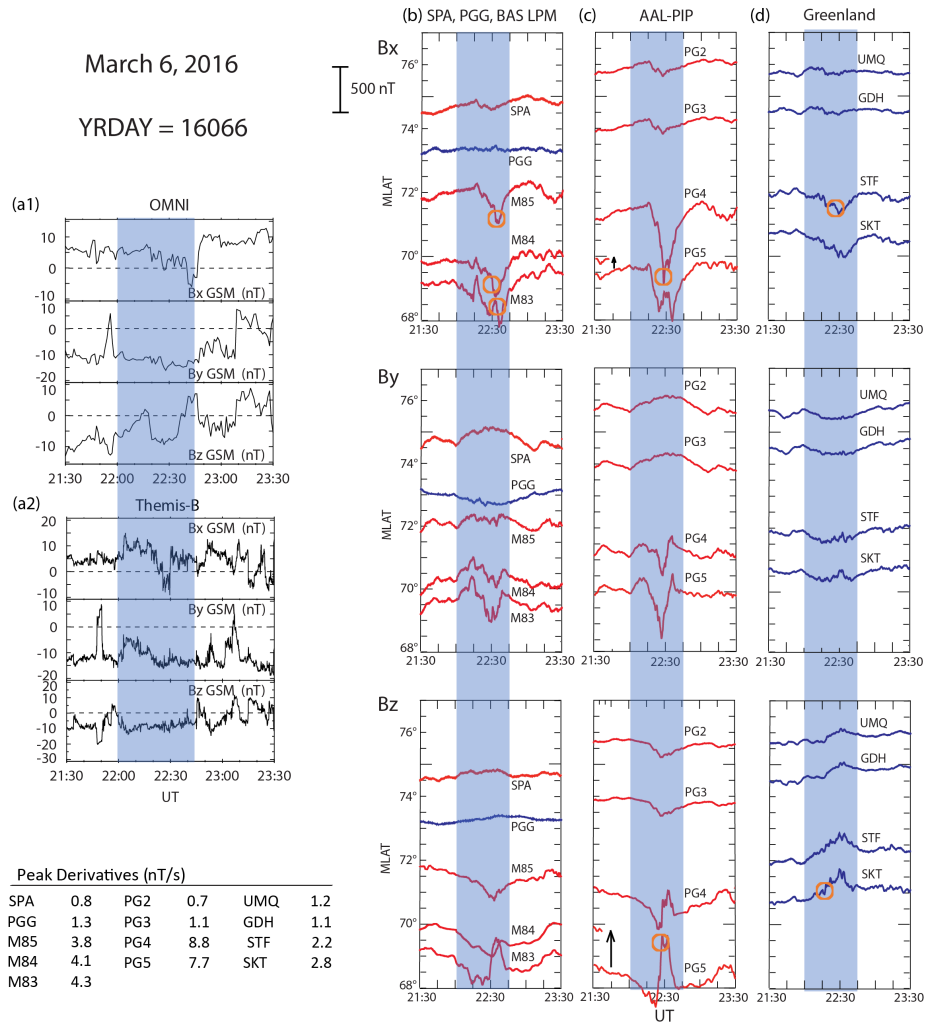


Figure 5: Composite figure showing IMF and high latitude magnetometer data from 2130 to 2330 UT March 6, 2016, as in Figure 2. Column (a) shows IMF data in GSM coordinates from the OMNI database and Themis B. A small orange circle is located near the largest derivative (if > 2 nT/s) at each station. The vertical arrows in panel (c) indicate that the B_x and B_z traces from PG5 have been shifted to lower latitude in order to not overlap the PG4 traces.

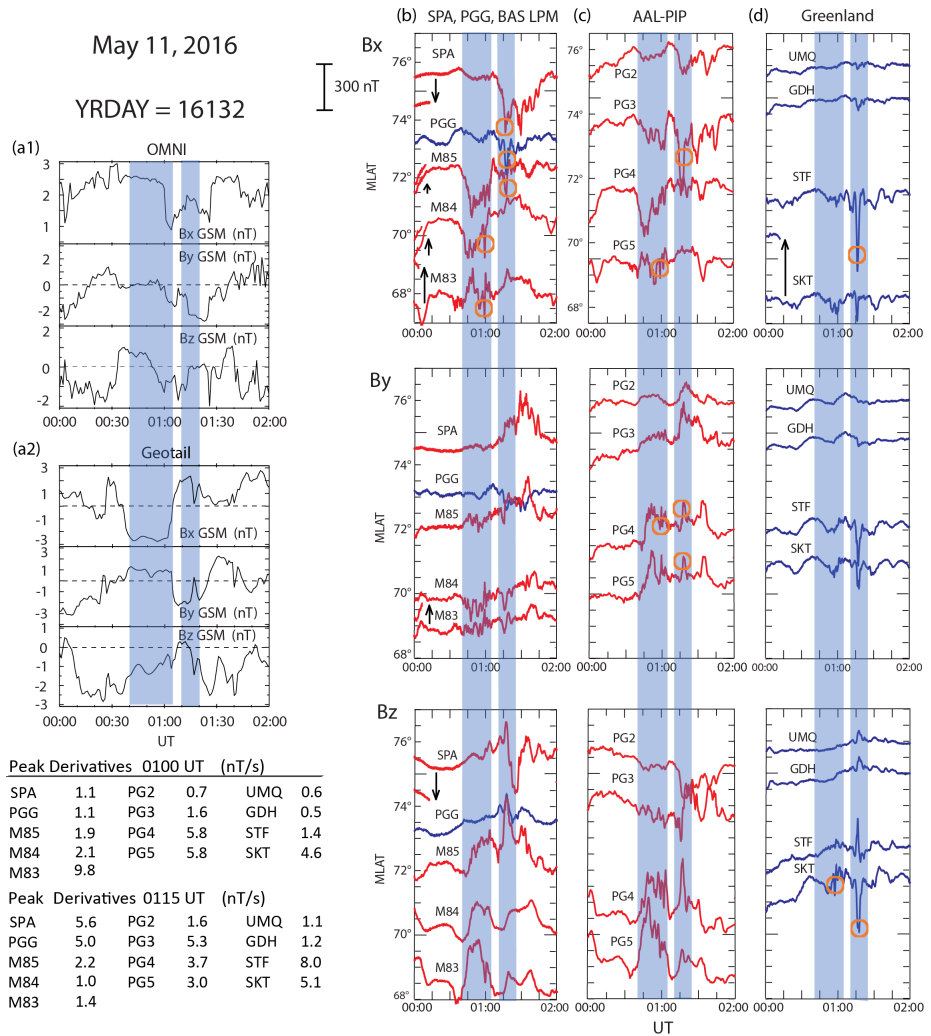


Figure 6. Composite figure showing IMF and high latitude magnetometer data from 0000 to 0200 UT May 11, 2016, as in Figure 2. Column (a) shows IMF data in GSM coordinates from the OMNI database and Geotail. A small orange circle is located near the largest derivative (if > 2 nT/s) at each station. The vertical arrows in panels (b) and (d) indicate that some of the traces from SPA, M83, and SKT have been shifted in latitude in order to not overlap the adjacent traces. Note also the different vertical scale for the B_x part of panel (b) than for panels (c) and (d).

North/South MPE Amplitude Ratios

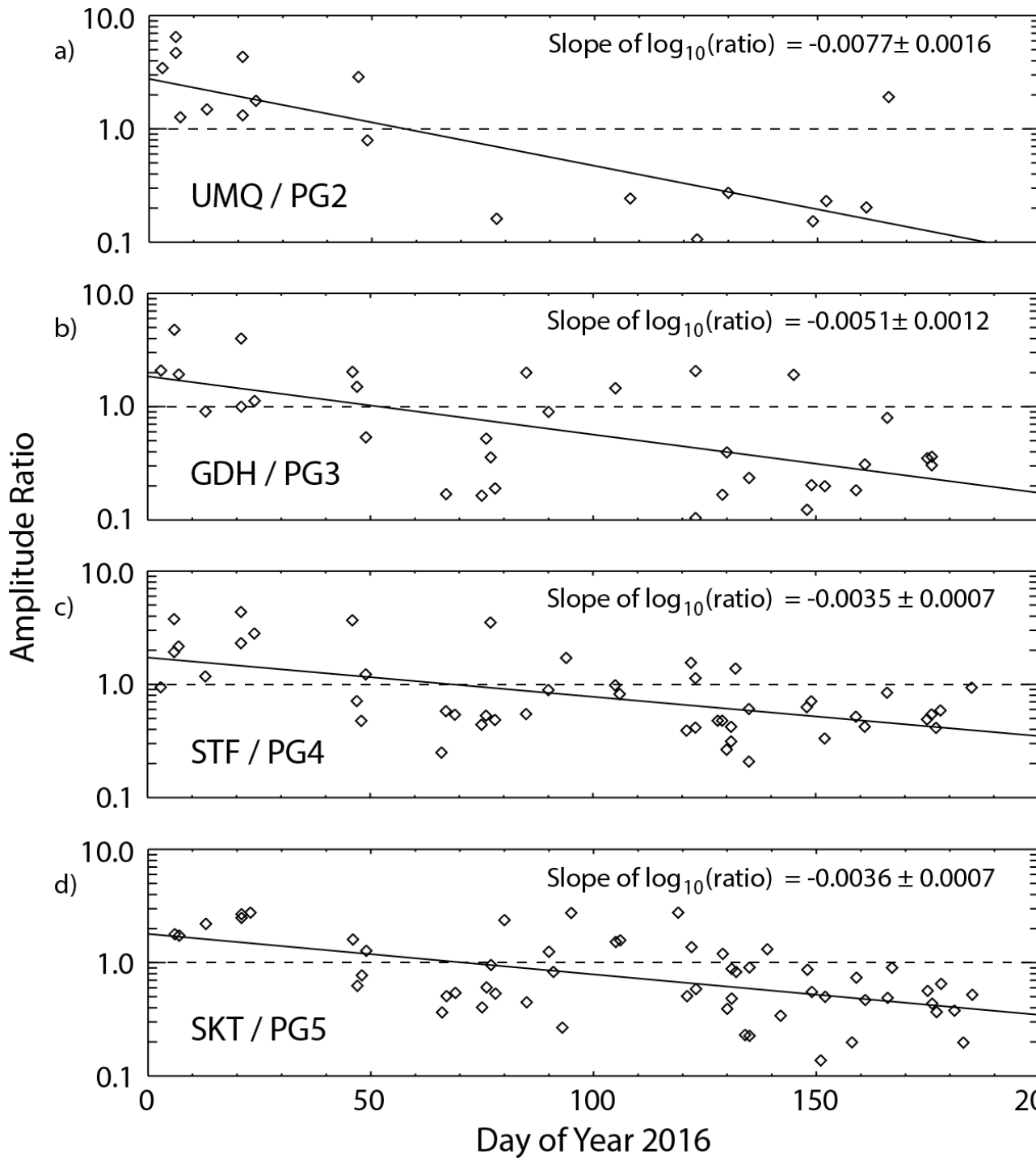


Figure 7. Plot of the ratio of MPE derivatives at northern and southern stations, $dB_N/dt / dB_S/dt$, as a function of the day of the year in 2016 for each of the four conjugate station pairs: a) UMQ / PG2, b) GDH / PG3, c) STF / PG4, and d) SKT / PG5. Only those events with at least one > 6 nT/s event at each station pair are shown.

Arctic / Antarctic MPE Amplitude Ratios: STF/PG4

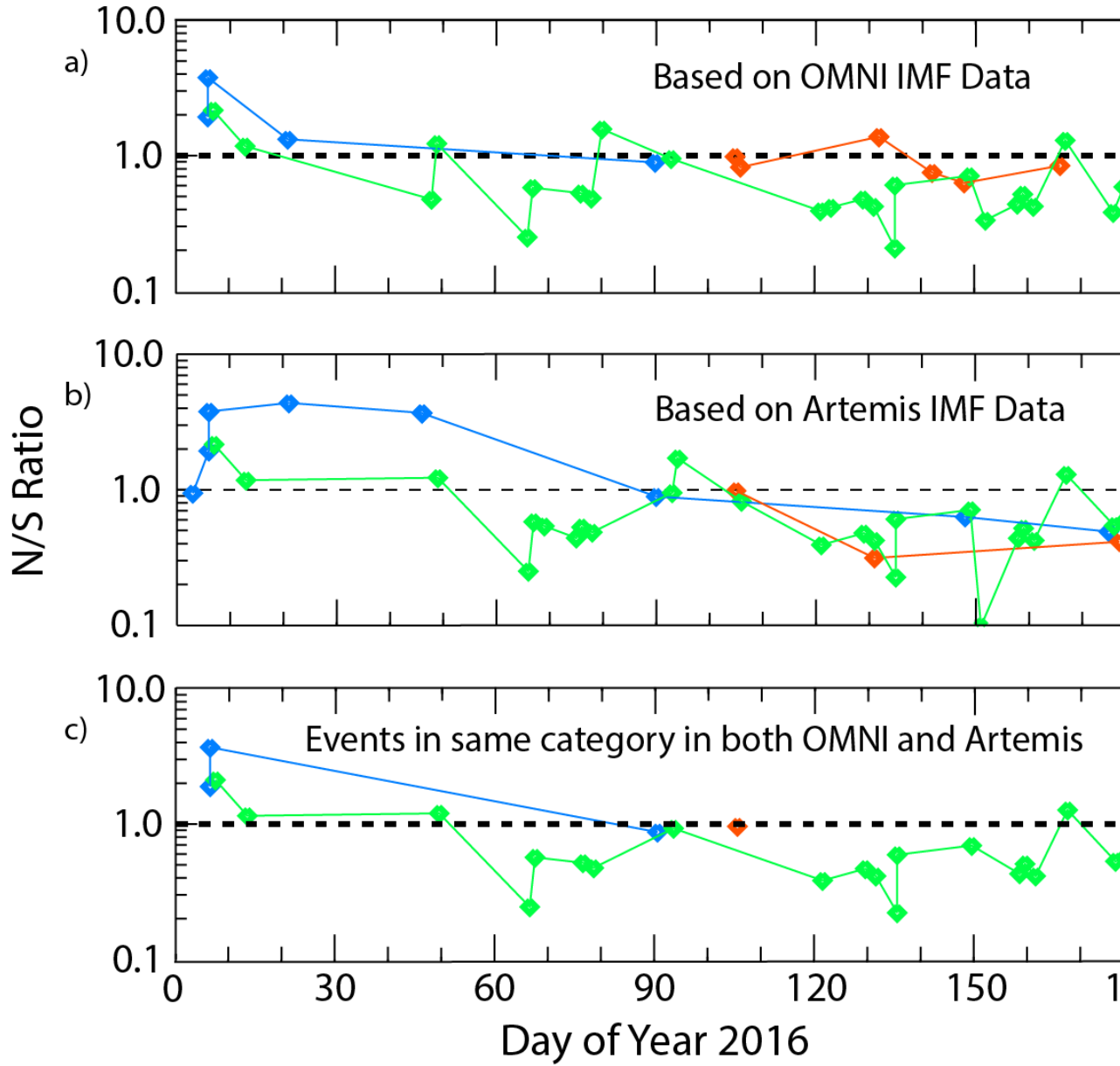


Figure 8. Plots of the ratios of amplitudes of MPE events observed at the STF/PG4 conjugate station pair during events preceded by an interval of at least 15 minutes of IMF $B_z < 0$ and IMF B_y being consistently either > 1 nT (blue), within 1 nT of 0 (red), or < -1 (green). Panels a) and b) show all

events for which OMNI data and Artemis/Themis IMF data satisfied these conditions, respectively, and panel c) shows only those events for which OMNI and Artemis/Themis data saw both consistent IMF $B_z < 0$ and the same category of consistent IMF B_y values.

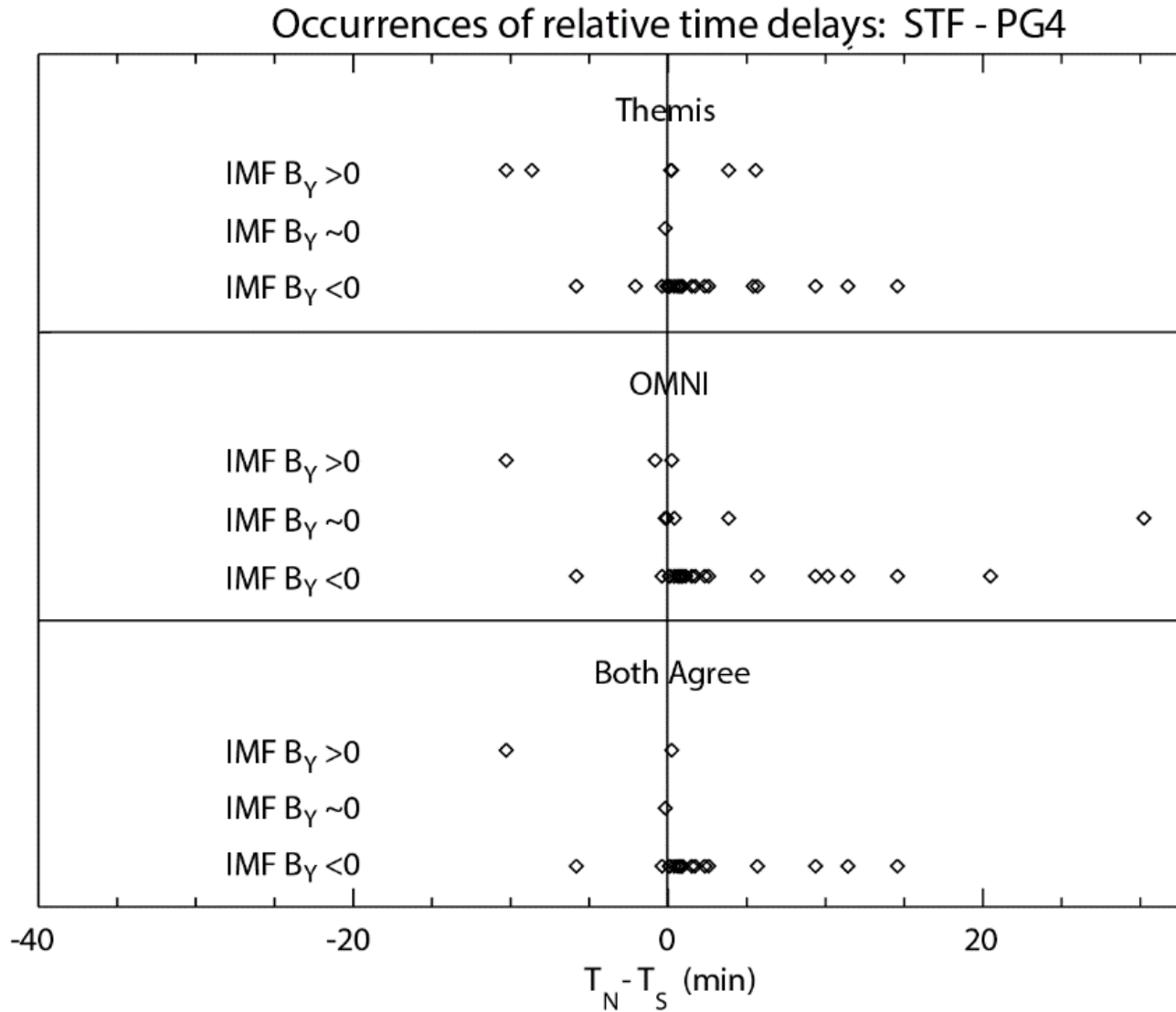


Figure 9. Plots of the distribution of time delays ($T_N - T_S$) between observations of the ΔB_x minima associated with each MPE event in at the STF - PG4 station pair. Panel (a) shows events with IMF $B_y > 1$, within ± 1 of 0, and < -1 , respectively, as measured by Artemis/Themis. Panel (b) shows events measured by OMNI, and panel (c) shows only those events for which Artemis/Themis and

OMNI IMF categories agreed.

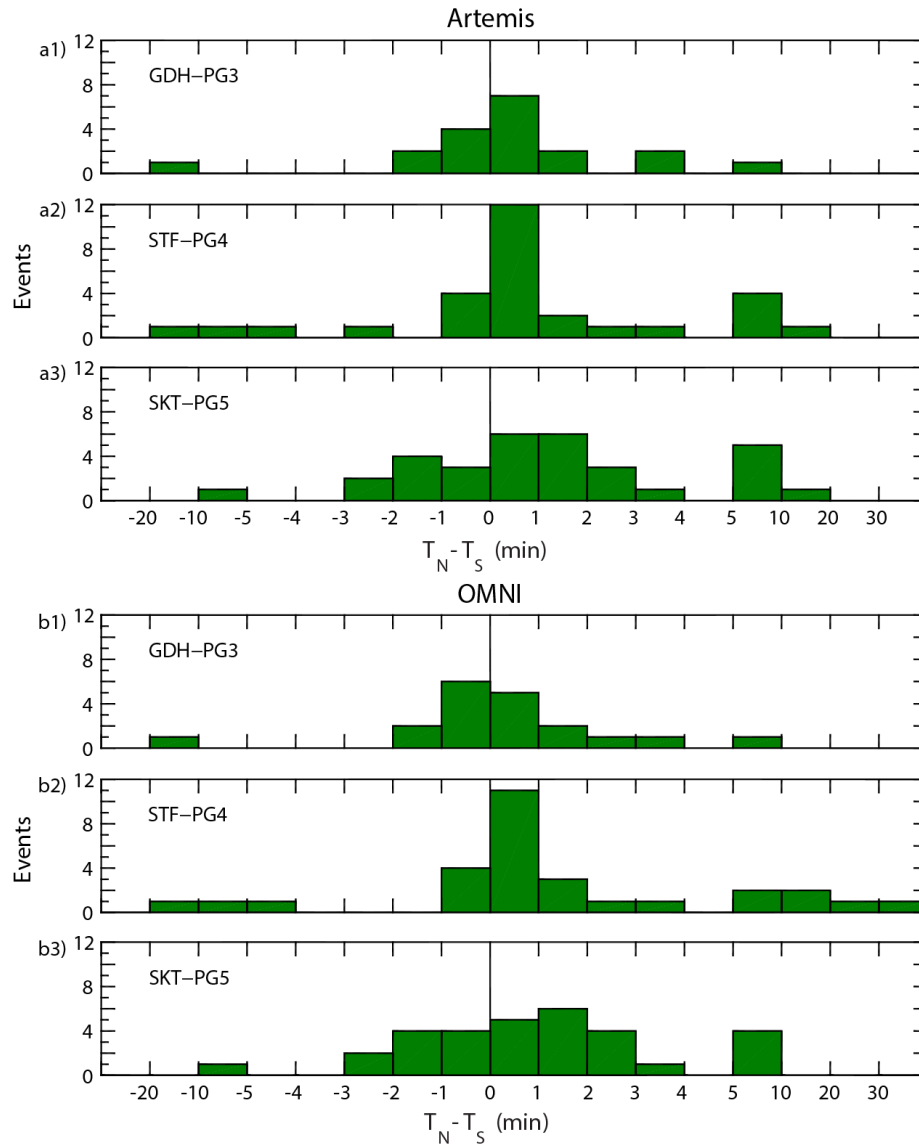


Figure 10. Histograms of the north-south time delay between MPE events observed at magnetically conjugate station pairs GDH – PG3, STF – PG4, and SKT – PG5, using events in all three categories of IMF B_y from a) Artemis/Themis data and b) OMNI data. Note the larger bin sizes beyond ± 5 minutes.

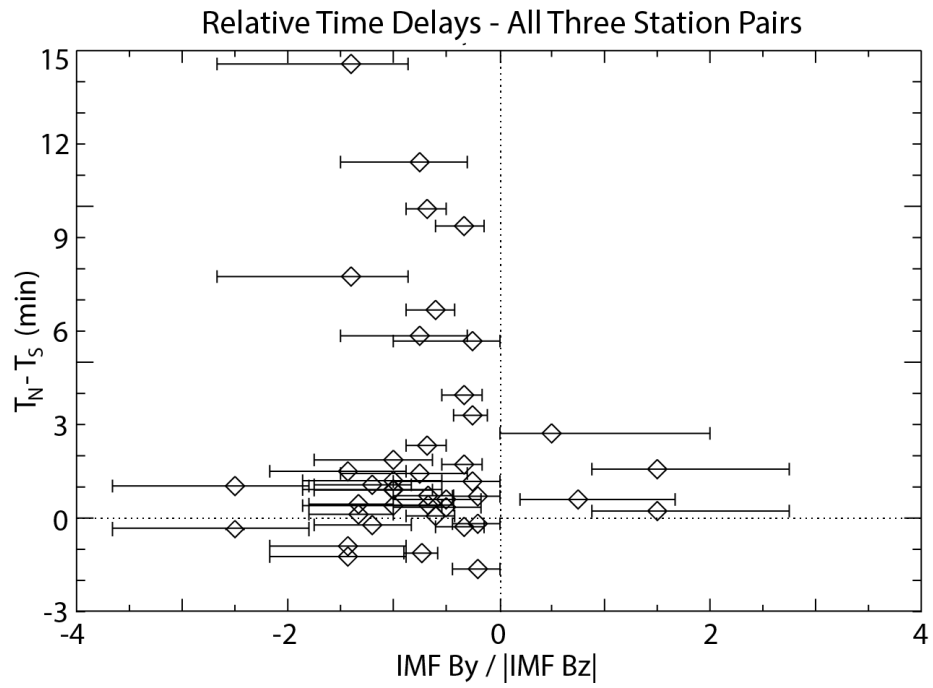


Figure 11. Plot of the time delay $T_N - T_S$ between minima in the B_x component at three conjugate station pairs (GDH-PG3, STF-PG4, and SKT-PG5) as a function of the IMF B_y/B_z ratio for all events where the signs of the IMF B_z and B_y components in the Artemis and OMNI data bases agreed.